Can Lensing Measure The Shape Of Dark Matter Halos?

by

Uzair Hussain

A thesis
presented to the University of Waterloo
in fulfillment of the
thesis requirement for the degree of
Master of Science
in
Physics

Waterloo, Ontario, Canada, 2012

I hereby declare that I am the sole author of this thesis. This is a true copy of the thesis, including any required final revisions, as accepted by my examiners.

I understand that my thesis may be made electronically available to the public.

Abstract

The aim of this project was to explore the shapes of dark matter halos using high resolution N-body simulations. One of the main aspects explored was how well the shape can be measured through weak lensing. To explore this, simulations were run using the GADGET-2 code [62] and a method used to measure ellipticities was tested [48]. It was found that Large Scale Structure along the line of sight diluted the measurements and made halos appear more spherical. On the other hand, substructure close to the halo introduced a bias where intrinsically elliptical halos appeared to be slightly more spherical and intrinsically spherical halos appeared to be slightly more elliptical. The effects of projection on concentration were also explored, it was concluded that halos which are most elliptical in 3D tend to appear the most concentrated in projection. Finally, we tested the possibility of using shape or concentration measurements to help break the degeneracy in Ω_M and σ_8. We found that this may be possible with $\sim$ 3000-4000 shape measurements or $\sim$ 400-500 concentration measurements.

Acknowledgements

I am extremely grateful to my supervisor Dr. James E. Taylor. This project would not have been possible without his patience, wisdom and diligent mentoring. And, of course, his unique sense of humor always helped to relieve stress. Further, I would like to acknowledge all my instructors; Dr. Mike Hudson, Dr. Achim Kempf, Dr. Brian McNamara, and again Dr. James E. Taylor, for their remarkable teaching ability.

I want to thank my committee members; Dr. Avery Broderick, Dr. Mike Fich and Dr. Mike Hudson, for taking out the time to read this thesis.

I would also like to thank all my peers and friends for their advice and support. Especially, David Aasen, Siavesh Aslanbeigi, Wilson Brenna, Kyle Broflovski, Eric Brown, Eric Cartman, Tyson DeNobrega, Adela Gherga, Chad Greene, Jonathan Grossauer, Laura Henderson, Robbie Henderson, Yasaman Kouchekzadeh, David Layden, Robert Jonsson, Danielle Leonard, Stan Marsh, Kenny McCormick, Paul McGrath, Angus Mok, Marius Oltean, Kyle Oman, Miok Park, Ryan Speller, Sean Stotyn, Paul Tiede, Samuel Tisi, Stephen Turnbull, Sara Venskates, Eric Webster, Anson Wong and anyone else who I missed.

A special thanks goes out to all my family members, especially, Ussrah Hussain and Adnan Akbar.

And lastly but most importantly I would like to thank my parents, without their support this would have been impossible.

To the current residents of Zarigul

Table of Contents

List of Tables

List of Figures

Chapter 1

Introduction

The current model that best describes the Universe is called the ΛCDM model. The model states that the universe we inhabit started of in a hot, dense state and expanded to what we see today. The Λ stands for the 'Cosmological Constant' and CDM is short for 'Cold Dark Matter'. The reason behind this choice of nomenclature is that Λ describes the expansion of the universe and CDM describes the invisible matter that galaxies are embedded in. The work of this thesis is focused on this CDM, specifically the shapes of the halos that the CDM collapses into, and how this shape maybe measured.

This thesis is organized as follows. The rest of this Chapter is dedicated to cover the necessary background from the literature. Section 1.1 describes some observations that are the basis of the ΛCDM model. Further, in Section 1.2 we briefly go through some of the mathematics of the ΛCDM model and explain how the structure in the universe today came to be. At the end of the chapter, in Section 1.3, we see how clusters of galaxies are important astronomical objects which are crucial for the development of cosmology.

In Chapter 2, other studies relevant to the shape of halos are discussed. Section 2.1 discusses an effective fitting formula for the density profile of halos, and how the 3-dimensional shape of halos is quantified. In Section 2.2 the importance of halo shapes is motivated. Further, in Section 2.3, some formalism for Gravitational Lensing, and how it fits into the

halo shape paradigm is discussed. In Chapter 3 some details of the N-Body Simulations and the methodology used in this project are provided. And finally, in Chapter 4 the results are discussed and some concluding remarks are provided.

1.1 Puzzling Jewels of Modern Cosmology

1.1.1 Hubble Flow & The Cosmological Constant, Λ

In 1929, Edwin Hubble published a paper where he showed a relationship between the redshifts (or velocities, since $z = v/c$) of galaxies and their distance [28]. What he discovered was a simple linear law[1]

$$v = H_0 r \tag{1.1}$$

where H_0 is now called the Hubble Parameter and the equation itself is called the Hubble Law. What this meant was that the galaxies that were further were moving away from us at a faster velocity. This does not mean that the Earth is in a special place but rather that the universe is undergoing an isotropic and homogeneous expansion [57].

As astonishing as an expanding universe is, what is even more appalling is a universe that expands at an accelerating rate. The strong evidence for this comes from studies done on distant supernovae which excluded a decelerating or static universe[51] [55]. This work won the 2011 Nobel Prize which was awarded to S. Perlmutter, B. P. Schmidt and A. G. Riess [45].

1.1.2 Dark Matter

This section follows [57] closely unless referenced otherwise

[1] Now well verified [57]

The surface brightness of spiral galaxies as a function of radius, R, is described by an exponential law,

$$I(R) = I(0) \exp\left(-\frac{R}{R_s}\right) \tag{1.2}$$

where R_s is a scale length. After a few scale lengths the stellar mass of the galaxy becomes constant and the velocity of the stars should fall of with radius according to Kepler's Law, which states that $v \propto 1/\sqrt{R}$. In 1970, Vera Rubin and Kent Ford were able to measure the velocities of stars in the M31 galaxy upto $R = 24\text{kpc} = 4\text{R}_s$. If a rotation curve[2] is produced with these velocities it does not show a $1/\sqrt{R}$ shape, but rather it is flat out to large radii. This is surprising as there isn't enough visible matter to provide the necessary gravitational attraction to keep the stars in orbit. It is now known that its not just M31 with this behavior, but most spiral galaxies show the same flat rotation curve. A hypothesis that solves this problem is the existence of Dark Matter.

In the Dark Matter paradigm, galaxies are embedded in halos which are made of dark matter which only interacts with baryonic[3] matter gravitationally, i.e, it does not emit or absorb any photons, hence the name. The halo is more extended than the galaxy and can thus provide the extra pull to maintain high velocities towards the edges. Rotation curves of spiral galaxies are not the only clue pointing towards dark matter.

More evidence for dark matter comes from clusters of galaxies. To appreciate this we need to briefly go over how masses of clusters are obtained. The steady-state virial theorem states that;

$$K = -\frac{W}{2} \tag{1.3}$$

where K is the kinetic energy and W is the potential energy. When this is satisfied for a system we say that it is *virialized*. For the case of galaxies we have,

$$\frac{1}{2} M \left\langle v^2 \right\rangle = \frac{\alpha}{2} \frac{GM^2}{r_h} \tag{1.4}$$

[2] A rotation curve is a plot of $v(R)$ versus R

[3] Normal matter, made of protons, neutrons and electrons

where $M = \sum m_i$, $\langle v^2 \rangle = (1/M) \sum m_i v_i^2$, $\alpha \approx 0.4$ for observed clusters and r_h is the half mass radius, i.e. it is the radius which contains half of the cluster's mass. Re-arranging for M, we have,

$$M = \frac{\langle v^2 \rangle \, r_h}{\alpha G}. \tag{1.5}$$

Unfortunately $\langle v^2 \rangle$ and r_h can not be known exactly. Only the velocities of the galaxies moving along the line of sight can be determined from their red shift. For the Coma cluster, for e.g., the mean red shift is $\langle z \rangle = 0.232$. This gives a radial velocity of $\langle v_r \rangle = c \, \langle z \rangle = 6960$ km/s. Assuming that the velocity dispersion is isotropic we have,

$$\left\langle v^2 \right\rangle = 3 \left\langle (v_r - \langle v_r \rangle)^2 \right\rangle = 2.32 \times 10^{12} \mathrm{m}^2 \ \mathrm{s}^{-2} \tag{1.6}$$

Since we do not know what the dark matter composition for the cluster is we assume that the mass-to-light ratio is constant with radius. So r_h is now the radius which contains half of the clusters luminosity which for the Coma cluster turns out to be, $r_h \approx 1.5$Mpc. Using Eq. 1.5 the mass of the Coma cluster is then;

$$M_{Coma} \approx 2 \times 10^{15} \ \mathrm{M}_\odot \tag{1.7}$$

whereas the mass of the stars in the Coma cluster is $M_{Coma,*} \approx 3 \times 10^{13}$ $\mathrm{M}_\odot$ and the mass of the gas is $M_{Coma,gas} \approx 2 \times 10^{14}$ $\mathrm{M}_\odot$, which means that $\sim 88\%$ of the matter is dark matter. Such calculations have been performed for many other clusters and the discrepancy in the Coma cluster is not unusual.

Another powerful way to probe masses of astrophysical objects is Gravitational Lensing. Einstein's theory of General Relativity predicts that massive objects bend the trajectories of light rays. This allows massive bodies to act as *lenses* for the light coming from some background sources. The effect of this lensing is manifest in the apparent shape distortion of the source. Fig.1.1a shows the cluster Abell 221; note the distortions that show up as luminous arcs of the background galaxies. These distortions can be analyzed to produce an estimate of the mass that causes the distortion, this is discussed in detail in Section 2.3. An interesting example of a lensing study is the Bullet Cluster [15]. The Bullet Cluster

(a) Abell 2218 [42]

(b) Bullet Cluster [42]

Figure 1.1: Lenses

is the name given to a system of two clusters that have just underwent a collision. Most of the visible mass of clusters is contained in the hot gas which emits X-rays and some mass is contained in the stars. As two clusters collide the stars should pass right through each other without many collisions. The gas on the other hand is denser and during a collision all the gas molecules will undergo random collisions. Hence, as seen in Fig 1.1b in red, the gas gets separated from the stars and is found in the middle. But, interestingly enough, lensing studies show that most of the mass is still found around the stars (shown in blue). Since the dark matter halo of each cluster is collisionless it is expected to pass right through itself as in the case of the bullet cluster. This provides very strong evidence for the existence of dark matter.

1.1.3 The Cosmic Microwave Background Radiation (CMB)

As the name suggests, the CMB is an observed isotropic radiation that permeates the universe. It was first observed in 1965 by A. Penzias and R. Wilson when they were working for Bell Laboratories. They discovered the CMB by accident as they were actually working on radio astronomy and telecommunication related problems [57]. They were awarded the

1978 Nobel Prize for this discovery [45]. Before the CMB was observed it was theorized that a universe which starts from a hot dense state would result in such a phenomena; why this is true is touched briefly in Section 1.2.2. Now the CMB is well measured thanks to WMAP [70] and Planck satellites [52].

1.2 The ΛCDM Model

1.2.1 The FRLW metric

This section follows [57] closely unless referenced otherwise

One of the exact solutions to Einstein's Field Equations is the FLRW[4] metric. It describes a homogeneous and isotropic expanding spacetime. Due to isotropy and homogeneity, the spacetime is either flat, everywhere positively curved or everywhere negatively curved. There is considerable evidence that suggests that the universe is flat [70]. The flat FLRW metric is given by,

$$ds^2 = -c^2dt^2 + a(t)^2[dr^2 + r^2d\theta^2 + r^2\sin^2\theta\, d\phi^2] \tag{1.8}$$

where $a(t)$ is the so-called scale factor, it plays the role of stretching or contracting space. Since the scale factor is not a constant there is some ambiguity associated with defining distance. There are two ways around this; the comoving distance and the proper distance. The comoving distance is the distance seen by a light ray, i.e, $ds^2 = 0$. From the metric this gives us;

$$c\int \frac{dt}{a(t)} = \int dr = r \tag{1.9}$$

So comoving distances are just the co-ordinate distances. But say an observer is interested in the distance at a particular instant in time. She has some tape measure she uses to measure distances which does not expand with space. What she measures with this tape

[4]Friedmann Lemaitre Robertson Walker metric

measure is called the proper distance, since time is fixed $dt = 0$, and the metric gives us;

$$d_p(t) = a(t) \int dr = a(t)r. \tag{1.10}$$

Taking a derivative with time of Eq. 1.10 gives us, $v_p(t) = \frac{\dot{a}(t)}{a(t)} d_p(t) = H(t)d_p(t)$, where we have defined the Hubble Parameter, $H(t)$. Note that this is the same equation, Eq. 1.1, that Hubble empirically derived and H_0 is the Hubble parameter today. A natural question to ask is what form does $a(t)$ have? It turns out that the answer to this question depends heavily on the densities of what the universe is made of.

There are three main ingredients of the universe, radiation, matter (dark and baryonic matter) and a cosmological constant, Λ. We define a quantity called the *density parameter* for any ingredient X by;

$$\Omega_X(a) = \frac{\epsilon_X(a)}{\epsilon_c(a)} \tag{1.11}$$

where $\epsilon_X(a)$ is the energy density at a certain scale factor. Say, we assume that there is only one ingredient X in the universe then $\epsilon_c(a)$ is a critical density such that if $\epsilon_X(a) > \epsilon_c(a)$ then the universe is positively curved, if $\epsilon_X(a) < \epsilon_c(a)$ then the universe is negatively curved and if $\epsilon_X(a) = \epsilon_c(a)$ then the universe is flat. It is important to know what form $\epsilon_X(a)$ has for each ingredient;

$$\epsilon_r(a) = \epsilon_{r,0} a^{-4} \tag{1.12}$$

$$\epsilon_m(a) = \epsilon_{m,0} a^{-3} \tag{1.13}$$

$$\epsilon_\Lambda(a) = constant \tag{1.14}$$

where subscripts r, m and Λ are for radiation, matter and the cosmological constant respectively. And $\epsilon_{X,0}$ is the present day density at $a = 1$. The power of -3 for the matter density is intuitive, as space expands the volume increases and the density falls as the volume increase. The same is also true of the radiation density, but since radiation is in the form of waves and the energy is inversely proportional to the wavelength an expanding space reduces the energy of the photons, hence the power of -4. Among the assumptions of homogeneity, isotropy and an expanding space if we add that $a(t)$ is a monotonically

increasing function then this gives us a crude time line of the universe; if at early times $a << 1$ then the universe is dominated by radiation. Then as the universe expands the radiation gets diluted and we enter a matter dominated epoch and once that gets diluted we are in a Λ-dominated universe.

But is $a(t)$ monotonically increasing? The answer to this comes from studying the solutions of the Friedmann equation which is given by;

$$\frac{H^2}{H_0^2} = \frac{\Omega_{r,0}}{a^4} + \frac{\Omega_{m,0}}{a^3} + \Omega_{\Lambda,0} + \frac{1-\Omega_0}{a^2} \tag{1.15}$$

where the $\Omega_{r,0}$, $\Omega_{\Lambda,0}$ and $\Omega_{m,0}$ are the density parameters at present day, $a = 1$. And Ω_0 is the sum of all the $\Omega_{X,0}$. From observations the current values[5] of the $\Omega_{X,0}$ parameters are;

$\Omega_{r,0}$	8.4×10^{-5}
$\Omega_{\Lambda,0}$	0.70
$\Omega_{m,0}$	0.30

Table 1.1: Approximate values of cosmological parameters

Using the above values, E.q 1.15 can be solved for $a(t)$. At early times the universe is radiation dominated with $a(t) \propto t^{1/2}$ at intermediate times it is matter dominated with $a(t) \propto t^{2/3}$ and at late times it is Λ-dominated with $a(t) \propto \exp^{Kt}$ where K is a constant. Note that the last term in E.q 1.15 determines the shape of the universe. If $\Omega_0 = 1$ then the universe is flat.

1.2.2 Clumps of Matter

The FRLW metric assumed that the universe was homogeneous and isotropic. But when one looks out into the night sky this is certainly not the case. It is only on very large scales, ~ 100 Mpc that the assumptions of homogeneity and isotropy work [57]. On smaller scales

[5] These are approximate see Table 3.1 for more accurate WMAP7 values.

we see much more complexity. From super-clusters and voids to rich clusters and galaxies and stars to planets. So how does all this structure come to be?

In the Big Bang model the universe is believed to have started from tiny quantum mechanical density fluctuations which exploded into a dense, rich, hot plasma of photons and elementary particles. At $\sim 10^{-36}$s to $\sim 10^{-34}$s the universe underwent very rapid exponential growth, called inflation [5], rapid enough that these tiny density fluctuations were stretched until they were no longer in causal contact. What does it mean to be in causal contact? In order to understand this we need to understand what is meant by a horizon. If we put limits of 0 and t on Eq. 1.9 we get the co-ordinate distance that a photon has traveled since the Big Bang. But to make the co-ordinate distance physical we need proper distances. This is done by multiplying with $a(t)$. Hence we have [57];

$$d_{hor} = a(t) \int_0^t \frac{cdt}{a(t)} \tag{1.16}$$

Because nothing travels faster than the speed of light, every point in space could only have been in *causal contact* by things within a sphere of d_{hor}. In the early universe the size of the horizon is very small. At $t \sim 10^{-36}$ the size of the horizon was, $d_{hor} \sim 6 \times 10^{-28}$m. A density perturbation that is bigger than the horizon will not be affected by pressure, viscosity, etc [49]. So, assume that there is some spherical density perturbation that has radius, $\lambda > d_{hor}$ and density, ρ_1 and the background as density, ρ_0. We also define the following density parameter,

$$\delta = \frac{\rho_1 - \rho_0}{\rho_0} \tag{1.17}$$

Because of spherical symmetry we assume that the perturbation evolves as a universe with spherical curvature, $\kappa = 1$. The Friedmann equation for such a universe can be written as [49],

$$H_1 + \frac{1}{a_1^2} = \frac{8\pi G}{3}\rho_1 \tag{1.18}$$

and the region outside is a flat universe with the Friedmann equation given by [49];

$$H_0^2 = \frac{8\pi G}{3}\rho_0 \tag{1.19}$$

We assume that both universes have the same Hubble parameter H and since the perturbation is small we assume $a_0 \approx a_1$. If subtract the two we get;

$$\delta = \frac{3}{8\pi G}(\rho_0 a^2)^{-1} \tag{1.20}$$

From the above equation we can know the evolution of super-horizon sized perturbations. In the radiation dominated phase we have $\rho_0 \propto a^{-4}$ and in the matter dominated phase we have $\rho_0 \propto a^{-3}$, this gives us;

$$\delta \propto a^2 \tag{1.21}$$

for the radiation dominated phase and,

$$\delta \propto a \tag{1.22}$$

for the matter dominated phase.

As the universe gets older and the horizon grows, these density perturbations or 'modes' enter the horizon. They are now in causal contact and effects of pressure become important. If a pressure gradient can build up fast enough then it will prevent the perturbation from growing. The characteristic time for pressure gradients to build up depends on the sound speed, c_s, of the material, since any changes in density will travel at the sound speed. The characteristic time for pressure build up is,

$$t_{pressure} \sim \frac{\lambda}{c_s} \tag{1.23}$$

The time for gravitational collapse can be estimated by the free fall time,

$$t_{freefall} \sim (G\rho)^{-1/2} \tag{1.24}$$

So condition for a perturbation to grow is, $t_{pressure} > t_{freefall}$. Or, $\lambda > c_s(G\rho)^{-1/2}$. This way we can define a critical radius for a density perturbation,

$$\lambda_J = \left(\frac{\pi c_s^2}{G\rho}\right)^{1/2} \tag{1.25}$$

Where the factor of π comes from a more rigorous treatment [49]. The above quantity is called Jeans length. Note that we know that the universe contains more than just one species of matter. In the case of multiple species, c_s corresponds to the species which has the density perturbation and ρ corresponds to the dominant species. Pressure build up is not the only process that prevents density perturbations from growing. If the universe expands fast enough it can stretch out perturbations inhibit and growth. To see this, note that the universe starts in an era of radiation domination. The time scale for the expansion of the universe is $t_{exp} \sim (G\rho_R)^{-1/2}$. A perturbation in the dark matter component would have $t_{freefall} \sim (G\rho_{DM})^{-1/2}$. Since at radiation domination $\rho_R > \rho_{DM}$, $t_{exp} < t_{freefall}$. Hence even if $t_{freefall} > t_{pressure}$ the perturbation cannot grow as a^2 and is inhibited.

So then let us follow the evolution of a dark matter mode with radius or wavelength λ. When the universe is in its early stages $\lambda > d_H$ or $a < a_{enter}$ the mode grows as $\delta \sim a^2$ as in Eq. 1.21. A more rigorous analysis from linear perturbation theory tells us that after photon-baryon modes have entered the horizon, during the radiation domination phase, the fluid oscillates and if a dark matter mode has $\lambda < d_H$ and it is evolving during this oscillatory period, it grows as $\delta \sim \ln(a)$. After this, as the radiation gets diluted the universe is in the matter dominated phase. This crossover happens at a scale factor a_{eq}, such that $\rho_R(a_{eq}) = \rho_{DM}(a_{eq})$. During the matter domination phase the dark matter perturbations then grow as $\delta \sim a$ as in Eq. 1.22.

But where do the baryons enter in this program? Unlike dark matter, baryons couple strongly to the photons. So their behavior is very similar to that of the photons. For modes $\lambda > d_H$ the growth is, $\delta_b \sim a^2$. For modes $\lambda < d_H$, during radiation domination, the baryons oscillate with the photons. Only at a later time when the expansion has made the universe cooler do the photons decouple from the electrons and protons. This era is called *decoupling*, it happens at redshift of around $z \sim 1100$. Right after decoupling happens the protons and electrons together with the other baryons start combining to make atoms, this era is called *re-combination*. At this point the universe becomes transparent as the photons can move freely. It is these very photons that we see in the CMB. Note that after decoupling, $\delta_b \sim a$. The interesting thing is that the size of structures seen today cannot

be accounted for if baryonic perturbations started to grow at $z \sim 1100$. But note that the dark matter perturbations have already been growing, they started growing effectively at a_{eq} which is $z \sim 3570$. So once the baryons get decoupled from the photons they fall into the dark matter halos that have been growing. This way the growth of the baryons is accelerated and the observed structure is accounted for [57].

Note that all the above are results from linear perturbations of the density field and are not accurate for $\delta \gg 1$, when the equations of motion become non-linear. To solve these non-linear equations then, N-Body simulations are required. Where the matter is simulated as a discrete set of N particles with a particular mass which depends on the volume and the number of particles used . Then the gravitational attraction on one particular particle due to all the other particles is calculated and its position is updated. This is done for all particles over some desired time. A more detailed account of these N-body simulations is provided in Section 3.1. As accurate as N-Body simulations are, they are computationally costly and there are some analytic models that have been developed that try to model the non-linear regime of the evolution of the density field. One of theses models is the spherical collapse model. As the name suggests, one of the main assumptions here is that the overdensity is spherically symmetric and evolves as a universe with density $\rho(r,t) = \rho_0(t)[1 + \delta(r)]$, note that $\delta(r)$ is a non-increasing function of r. The model relies on calculating the motion of each spherical shell at position r_i that contains some mass M_i interior to it [49]. The prediction for density contrast is,

$$\delta = \frac{9}{2}\frac{(\theta - \sin\theta)^2}{(1 - \cos\theta)^3} - 1 \tag{1.26}$$

where θ here is a function of t, i.e., $t \sim (\theta - \sin\theta)$ and increases as t increases. Hence, θ will be used as our measure of time. For early times $\theta \ll 1$ the prediction from linear perturbation theory is recovered, $\delta_{lin} \sim t^{2/3} \sim a$ as in Eq. 1.22. There are some important features of the evolution of δ. The point of maximum expansion is at $\theta = \pi$ and at this point the overdensity starts to collapse. The value of the overdensity is $\delta(\pi) = 4.6$, whereas, $\delta_{lin} = 1.06$ [49]. Theoretically, the model suggests that collapse occurs at $\theta = 2\pi$, but collapse to a singularity only occurs if the region is perfectly spherically symmetric.

Usually this is not the case and we get a virialized structure. Note also that linear prediction is $\delta_{lin}(2\pi) = 1.69$ [49]. Recall that the condition is Eq. 1.3. The potential of a spherically symmetric uniform density sphere is;

$$U = -\frac{3}{5}\frac{GM^2}{r} \tag{1.27}$$

At the moment of maximum expansion there is no kinetic energy and $K = 0$ and the total energy, $E = U = -(3/5)GM^2/r_{ta}$, where r_{ta} is called the turnaround radius. When the structure is virialized we have $U = -2K$ and $E = -K$. So then the *virial velocity*, is given by;

$$v_{vir} = \sqrt{\frac{6}{5}\frac{GM}{r_{ta}}} \tag{1.28}$$

and we have the relationship,

$$r_{vir} = r_{ta}/2. \tag{1.29}$$

Given the above relationship the density of the collapsed structure can be approximated as $\rho_{coll} = 8\rho_{ta}$.

1.2.3 Statistics of Large Scale Structure

This section very briefly introduces some of the mathematics involved in the statistics of large scale structure. Say we have some function $F(\mathbf{x})$. We can take the Fourier transform of the function and write it as $F(\mathbf{x}) = \sum F_{\mathbf{k}} e^{i\mathbf{k}\cdot\mathbf{x}}$. If we generalize this sum to an integral we have [50];

$$F(x) = \frac{V}{(2\pi)^3}\int F_k(k)\exp(-i\mathbf{k}\cdot\mathbf{x})d^3k \tag{1.30}$$

where,

$$F_k(k) = \frac{1}{V}\int F(x)\exp(i\mathbf{k}\cdot\mathbf{x})d^3x \tag{1.31}$$

We can also expand the density field δ in a similar way;

$$\delta(\mathbf{x}) = \frac{V}{(2\pi)^3}\int \delta_k(k)\exp(-i\mathbf{k}\cdot\mathbf{x})d^3k \tag{1.32}$$

Here $|k| = 2\pi/\lambda$, where λ is the wavelength of a certain mode, as in the previous section. The variance of $\delta(\mathbf{x})$ is real and is given by;

$$\left\langle |\delta_k|^2 \right\rangle = \left\langle \sum_k \sum_{k'} \delta_k \delta^*_{k'} \exp(-i\mathbf{k}\cdot\mathbf{x}) \exp(-i\mathbf{k}'\cdot\mathbf{x}) \right\rangle \tag{1.33}$$

If we invoke orthogonality in the average, the $k \neq k'$ modes cancel out. Then, changing the sum over k to an integral;

$$\left\langle |\delta_k|^2 \right\rangle = \frac{V}{(2\pi)^3} \int |\delta_k|^2(k) 4\pi k^2 dk \tag{1.34}$$

where the condition of isotropy introduces the $4\pi k^2$. The quantity $|\delta_k|^2 = P(k)$, where $P(k)$ is called the power spectrum. We define the variance per $\ln(k)$, $\Delta^2(k)$, such that $\langle |\delta_k|^2 \rangle = \int \Delta^2(k)(d\ln k)$;

$$\Delta^2(k) = \frac{V}{(2\pi)^3} 4\pi k^3 P(k) \tag{1.35}$$

As we will see in further sections, it is useful to convolve the density with a filter. A useful filter is a top-hat filter,

$$f = \frac{3}{4\pi R_{TH}^3} \times \begin{cases} 1 & r \leq R_{TH} \\ 0 & r > R_{TH} \end{cases} \tag{1.36}$$

This way we can smooth out the density field for comparison with structures of a given size R_{TH}. The smoothed or filtered version of the density field is then given by;

$$\delta_{R_{TH}}(\mathbf{x}) = \int \delta(\mathbf{y}) f(\mathbf{x}-\mathbf{y}) d^3y \tag{1.37}$$

The variance in this density field is then,

$$\sigma_{R_{TH}} = \left\langle |\delta_{R_{TH}}|^2 \right\rangle = \int_0^\infty \Delta^2(k) |\tilde{f}(k)|^2 d(\ln k) \tag{1.38}$$

where $\tilde{f}(k)$ is the Fourier transform of f.

1.3 Constraining Cosmology Through Clusters

1.3.1 Mass Function

The mass function at a certain redshift gives the number of virialized halos in the mass range from M to $M + dM$. Press and Schecter (PS) [54] derived a mass function under the assumption that the number of halos can be found be studying the smoothed version of the density field, δ. This smoothing is done by applying a filter, as in Eq. 1.37. The radius of this filter corresponds to the expected size of the structure with mass M. The variance can also be computed by using Eq. 1.38, a commonly used smoothing size is 8 Mpc/h and is denoted as σ_8. The form that the PS mass function takes is given by [9];

$$\frac{dn(M,z)}{dM} = \sqrt{\frac{2}{\pi}} \frac{\bar{\rho}}{M^2} \frac{\delta_c}{\sigma_M(z)} \left| \frac{d \log \sigma_M(z)}{d \log M} \right| \exp\left(-\frac{\delta_c^2}{2\sigma_M(z)^2} \right) \tag{1.39}$$

where δ_c is a critical density, such that objects with mass M are formed from the parts of the smoothed density field, δ_M, that have $\delta_M > \delta_c$. $\sigma_M(z)$ is the variance for the mass scale M which has been linearly extrapolated, i.e., $\sigma_M(z) = D_+(z)\sigma_M$. Here $D_+(z)$ is called the growth function of the density field, for e.g. in the linear regime of the matter dominated era $D_+ \sim a = (1+z)^{-1}$ where the identity $1 + z = a(t_0)/a(t) = 1/a(t)$ has been used and the present day scale factor is $a(t_0) = 1$. Also note that $\bar{\rho}$ is the mean density of the universe. The PS mass function was proposed in 1974 and has served as a very important tool, but since then there have been more accurate versions of the mass function that have been calibrated by N-Body numerical simulations [9]. These new versions are realized as corrections to PS.

The theoretical mass function can be compared with an observational mass function to constrain cosmological parameters. The observational mass function is constructed by counting nearby clusters, which being massive, fall in the exponential tail of Eq. 1.39 [9]. Recall that in smoothing the density field to obtain δ_M a filter is applied and the procedure for applying the filter involves a convolution as described in Eq. 1.37. Note that this depends on a length scale, R, which is assumed to be the size of the structure

with a certain mass M, which in this case is R_{TH}. But the calculation of R depends on both M and Ω_m, i.e., $R \propto (M/\Omega_m \rho_c)^{1/3}$. The result of this dependence is that the mass function can only constrain a relationship in between σ_8 and Ω_m. Current cosmological surveys suggest that $\sigma_8 \Omega_m^{\alpha} = 0.4 - 0.6$ where, $\alpha \approx 0.4 - 0.6$ [9]. One of the key aspects of this thesis is to explore if and how shape measurements can help towards alleviating this degeneracy.

1.3.2 Shape, Age, Ω_M and σ_8

In Section 1.2.2 we saw briefly how dark matter collapses into halos. The mathematics used to describe this used the perturbed fluid equations in an expanding medium as a starting point. This serves as a good approximation, especially for earlier times. As has been mentioned previously, at late times the situation is more complicated. The collapse of a halo into a virialized structure is not a trivial process. To see this, we consider a *perfectly* spherically symmetric distribution of mass collapsing under its own gravity. We also assume that the velocity field is zero everywhere at $t = 0$. Clearly, as this system evolves the ultimate outcome is a singularity at $r = 0$. Since halos don't collapse in such an ideal manner we have to consider more realistic scenarios. It is very likely that the collapse we are considering will not be spherically symmetric and have some dispersion for the initial velocity. As a system like this collapses the ultimate outcome is not a singularity but a *virialized* structure. Towards the end of Section 1.2.2 we briefly talked about a model that describes halo collapse in the non-linear regime. But the best case for collapsing halos comes from N-Body simulations, where we see a scenario thats more realistic.

From the snapshots of theses simulations one sees that there is a whole web of cosmic structure, complete with filaments, sheets and halos. One need only look at the pictures of the Millennium Simulation to verify this [41]. One can see that each massive halo is connected to and fed by filaments in its environment. Also orbiting are subhalos which slowly lose mass to the main halo by tidal stripping. Mergers are seen, as two or more halos of comparable masses mix together and form bigger halos. The halos caught in between

all these complex physical processes are not spherical at all. If they closely resemble any well-defined geometrical shape, then that would be of an ellipsoid. This can be seen in Fig. 2.1.

As complex as the picture painted above is, these halos eventually relax [67]. Even if the halo is collapsing at different rates along different axes, which gives it its ellipsoidal shape, eventually as the halo gets *old* it virializes. Once it reaches the condition of Eq. 1.3 it is more spherical. Hence, the *age* of the halo is related to the halo's shape. This relationship between age and shape is motivated more in Chapter 2, where we verify that older halos tend to be more spherical and younger halos tend to be more ellipsoidal.

Recall that when we visited the PS function we encountered the growth function $D_+(z)$. This is a function that is a result of linear perturbation theory and it determines how the contrast in the density field δ grows. Note the assumption here is that when one decomposes the density field into its Fourier modes, as in Eq. 1.32, each individual mode evolves separately. This is why the pattern of the density field does not change but rather only increases in contrast at a rate determined by the growth function [50]. An exact solution for $D_+(z)$ is the following [9];

$$D_+(z) = \frac{5}{2}\Omega_m E(z) \int_z^\infty \frac{1+z'}{E(z')} dz' \tag{1.40}$$

where,

$$E(z) = \sqrt{\Omega_M(1+z)^3 + (1-\Omega_M-\Omega_\Lambda)(1+z)^2 + (1+z)^{3(1+w)}\Omega_\Lambda} \tag{1.41}$$

Note that $E(z)$ is just a more general version of E.q 1.15 where the identity, $1+z = a(t)^{-1}$, is used, and the w is the equation of state parameter for Λ. There is strong dependence of $D_+(z)$ on Ω_M, see Fig. 1 in [9] for example, there we can see that the growth rate, $D_+(z)$, increases much faster as a function of z to its present day value of unity for models with $\Omega_M = 1$ as compared to the model with $\Omega_M = 0.3$, with the model with cosmological constant, $\Omega_M = 0.3$ and $\Omega_\Lambda = 0.7$ being the intermediate [9]. Hence we see that how rapidly halos grow is sensitive to the growth factor $D_+(z)$ which is sensitive to Ω_M.

Another important quantity in cosmology is σ_8 which is the mean variance of the density field smoothed with a top hat filter with $R_{TH} = 8$ Mpc/h. A value of 8 Mpc/h was chosen because early observations yielded $\sigma_8 = 1$ [50]. Now this value is more accurately determined to be $\sigma_8 \sim 0.8$. In the literature one often encounters σ_8 referred to as the 'normalization'. This is in context to the normalization of the power spectrum. Once the value of σ_8 is constrained the normalization of the power spectrum, $P(k)$, can be set through Eq. 1.38. Recall that the power spectrum tells us how much 'power' there is at each length scale, $k \propto 1/r$. So, the normalization of the power spectrum determines how high the peaks are and how low the troughs are in the initial density field which eventually grows according to $D_+(z)$.

Now clearly, we only have one particular model of the universe which is the one we live in. We have already seen in the previous section that there is a degeneracy between Ω_M and σ_8. Another way to look at this is that when we construct a mass function just by counting clusters there is little information about how old the halo is, or how relaxed it is, or how fast it grew, or how big were the initial peaks that it grew from. These last two pieces are crucial, since we only have one particular universe out to $z \sim 1$ (for current cluster observations) one cannot accurately determine if the halos grew really fast or if they grew slowly but with a higher normalization because both can result in the same mass function for clusters close to the present day. If high redshift history is not known then it is not possible to break this degeneracy, at higher redshifts, the mass function becomes more sensitive to the underlying cosmological model [9].

This is where shapes of halos could provide a remedy. As discussed in the beginning of this section, once a halo collapses and has enough time to relax, i.e. get virialized then it is expected to be more spherical. If the power spectrum has a higher normalization then σ_8 is high and Ω_M is lower. This means that halos have not grown rapidly but rather have experienced a slower growth. In the converse case, if the power spectrum has a lower normalization then σ_8 is lower and Ω_M is high and halos have undergone a rapid growth. If halos grow slowly that means that they are older, and have had more time to relax, virialize and become spherical. If halos grow rapidly they do not get enough time to relax

and are likely to be ellipsoidal. As we will see in later chapters, one of major objectives of the research carried out for this thesis is to test this effect of shape, Ω_M and σ_8.

1.3.3 How Do Astronomers Build A Cluster Sample?

Clusters of galaxies can be detected in several ways. In the X-ray wavelength we see emissions from Intra-cluster Gas (ICM). In the optical and IR-band we see emissions from stars. Another detection method comes from distortions in the CMB caused by the Sunyaev - Zel'dovich effect and of course as we seen earlier with the example of the Bullet Cluster, through gravitational lensing [5]. The rest of this section briefly describes some of these detection methods.

X-ray Emission

The first detection of X-rays from a cluster came on 1977 from the High Energy Astronomical Observatory satellites. As mentioned above the source of the X-rays is from the gas that gets heated in the potential well of the clusters, reaching temperatures of about 10^6 - 10^8 K [2]. The physics behind this emission is thermal Bremsstrahlung. This is caused, loosely speaking, by the free electrons in the gas getting decelerated by ions and emitting photons. Following is an image of the Coma cluster form the ROSAT survey, which shows the X-ray emission;

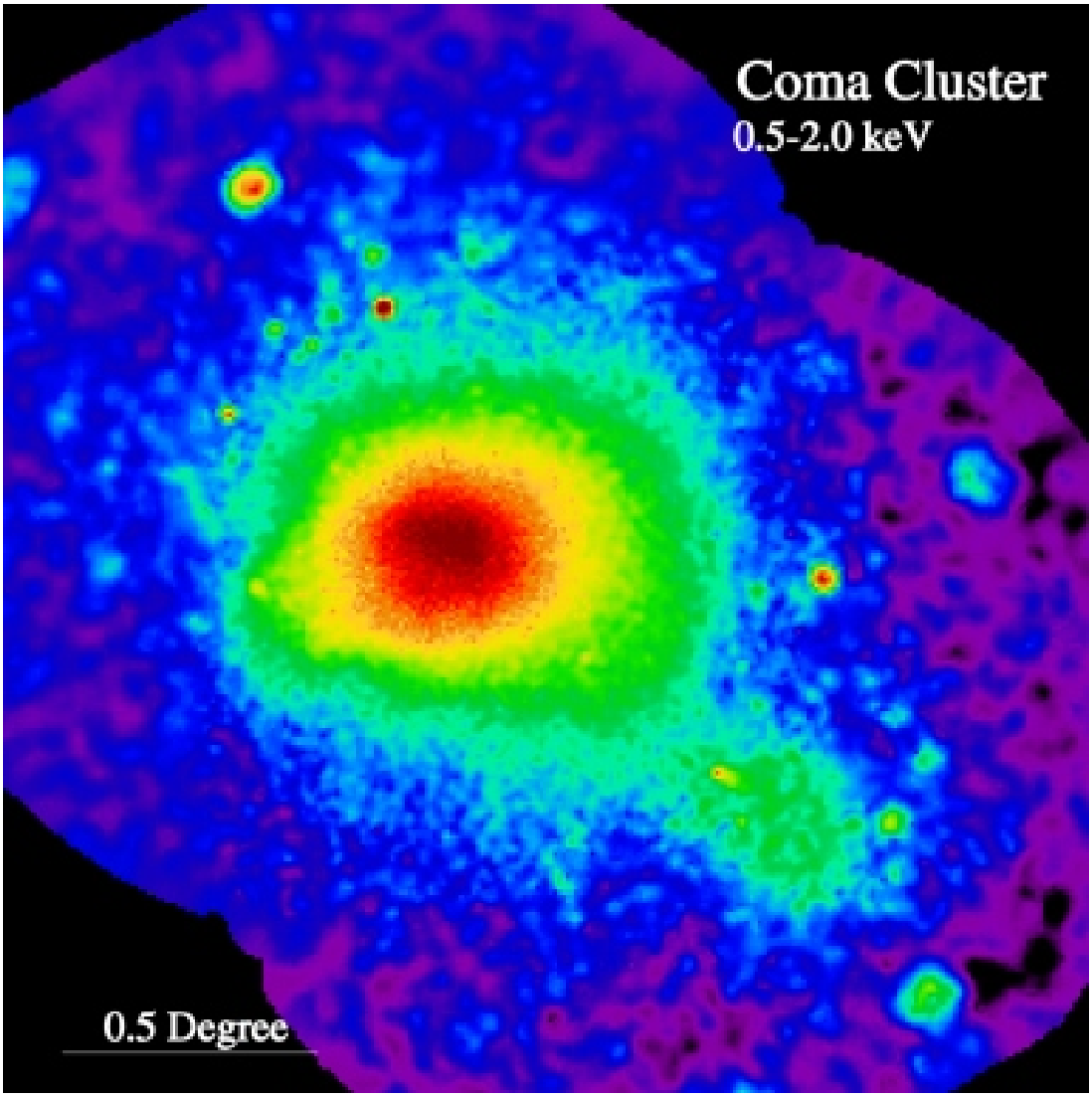

Figure 1.2: X-rays from the Coma Cluster [56]

Other than aiding the detection of clusters in the X-ray band, the ICM can also serve as a useful proxy for the mass of the cluster. If one assumes hydrostatic equilibrium of the gas and gravitational force of the cluster then we have [9];

$$\nabla P_{gas} = -\rho_{gas} \nabla \phi \tag{1.42}$$

where P_{gas} is the pressure of the gas and ρ_{gas} is the density and ϕ is the gravitational potential. If we assume spherical symmetry we get;

$$\frac{dP_{gas}}{dr} = -\rho_{gas}\frac{d\phi}{dr} = -\rho_{gas}\frac{GM(<r)}{r^2} \tag{1.43}$$

Further, if we invoke the ideal gas equation we arrive at the following,

$$M(<r) = -\frac{r}{G}\frac{k_B T}{\mu m_p}\left(\frac{d\ln\rho_{gas}}{d\ln r} + \frac{d\ln T}{d\ln r}\right) \tag{1.44}$$

where μ is the mean molecular weight, k_B is Boltzmann's constant, T is the temperature and m_p is the mass of the proton. By assuming power-law profiles for the gas density and temperature one can constrain the mass of the cluster. See for e.g. [64] [4]. There have also been model-independent studies done when the data is of very high quality, for e.g. [46].

Optical

Detection in the Optical or IR-band is based on a richness criteria of the galaxies found in the cluster. Early searches for clusters in the optical band have were one just by visual inspection, an example of this is the Abell sample [9]. But since the advent of CCD imaging more advanced algorithms can be used to find clusters, an example of this is [53]. Following is an image of the central region of the Coma Cluster, showing some dwarf galaxies. The image is constructed from optical data from the Sloan Digital Sky Survey (blue) and from the infrared data (red and green) from NASA's Spitzer Space Telescope;

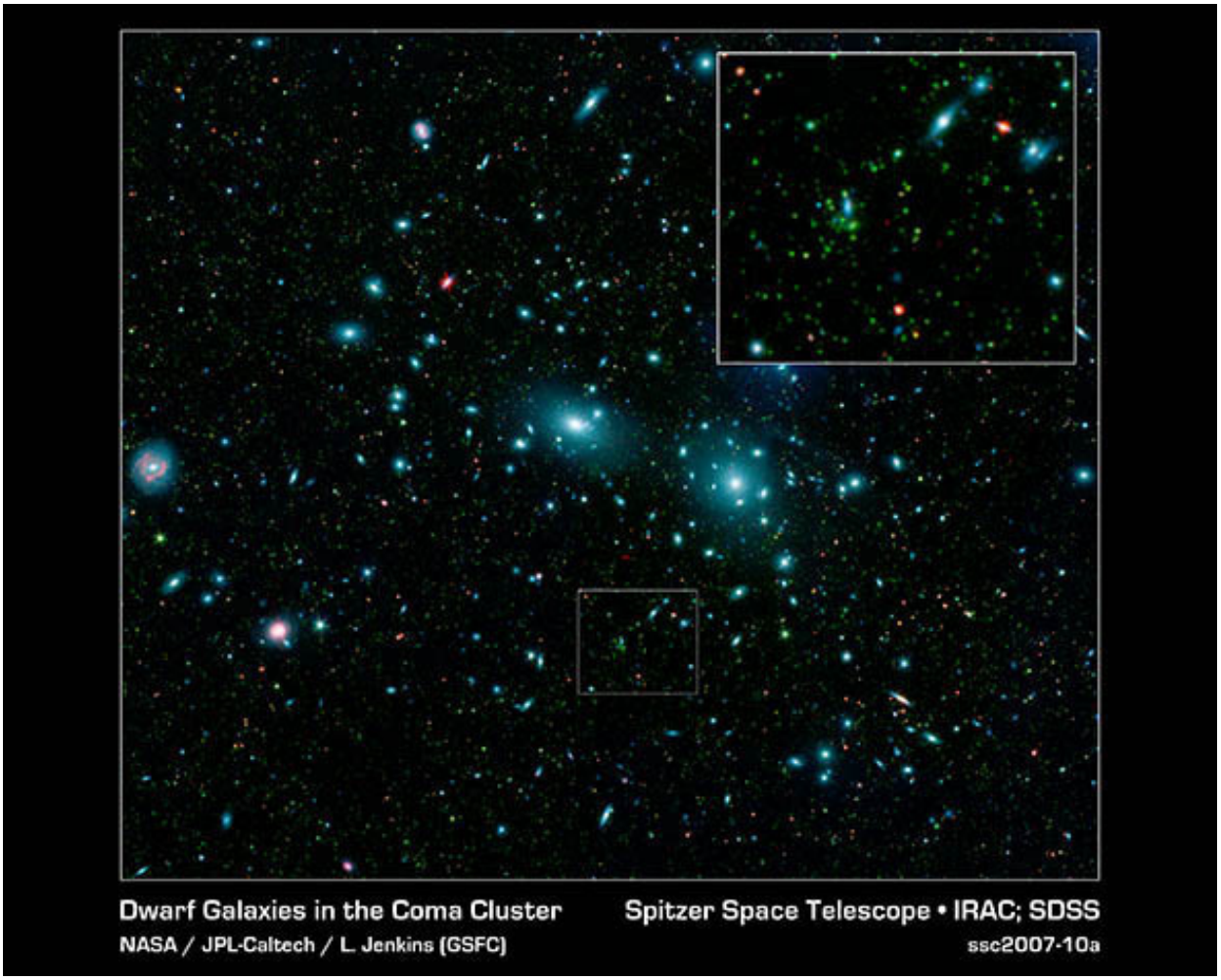

Figure 1.3: Coma Cluster in the optical and IR band [61]

The SZ-effect

Another means of detection of clusters is through the Sunyaev - Zel'dovich effect or SZ-effect for short. The physical mechanism by which this effect occurs is inverse Compton scattering. This is when a photon gains energy as it is deflected by an high energy electron. In the context of clusters of galaxies, the high energy electrons are provided by the gas in the ICM and the photons that receive the energy kick are the CMB photons. This produces distortions in the CMB map which can be analyzed to detect clusters. The main advantage of SZ detection over X-ray detection is that SZ does not suffer from flux dimming, $f \propto d_L^2(z)$. But the main obstacle in the way of accurate SZ detection is the interference in the signal due to foreground and background structures. One example of a study that explores these effects through high resolution N-Body simulations is [66]. Gas found in the filaments of large scale structure is unlikely to cause interference due to its relatively low density and temperature, but smaller halos may be a significant source of interference [9]. Current SZ-surveys include data from the South Pole Telescope [14] [63], the Atacama Cosmology Telescope [35] [37], and the Planck satellite [1].

1.3.4 Scaling Relations

If we assume that gravity is the only factor that effects the thermodynamics of the ICM then we can make predictions for how properties of clusters scale. Say we define M_{Δ_c} within a radius R_{Δ_c} such that, $M_{\Delta_c} \propto \rho_c(z)\Delta_c R_{\Delta_c}^3$, where ρ_c is the critical density and Δ_c is a mean density. Then if we assume hydrostatic equilibrium then we have for mass and temperature[9],

$$M_{\Delta_c} \propto T^{3/2} E(z)^{-1} \tag{1.45}$$

where $E(z)$ is given by Eq. 1.41.

If we assume further that the density of gas is a tracer of the dark matter density, $\rho_{gas} \propto \rho_{DM}$, and L_X is the thermal Bremsstrahlung luminosity corresponding to ρ_{gas} then

we have the following relation[9],

$$L_X \propto M_{\Delta_c} \rho_c T^{1/2} \propto T^2 \tag{1.46}$$

As for the SZ-effect the scaling relation is given by [9];

$$y_0 \propto T^{3/2} E(z) \propto L_X^{3/4} E(z)^{1/4} \tag{1.47}$$

where y_0 is called the Compton y-parameter and is the main observable in SZ-studies. These scaling relations are based of a very simple model of gravity being the sole driving force for the ICM, at all scales and redshifts. When they are tested against data from observations there is significant scatter which is a sign of more complex physics involved [9].

Using these relations of the observables a mass function is constructed and compared with theoretical predictions to constrain the density parameter Ω_M and the normalization σ_8. Constraining cosmology in this manner is a very active field and is only indirectly related to the contents of this thesis, hence, most of the details are omitted. A more thorough account of the technical details, especially of the degeneracy and uncertainties associated with constraining Ω_M and σ_8, can be found in reviews like [9] and [2].

Chapter 2

The Shape of Halos

2.1 Dark Matter Halos

2.1.1 The NFW Profile

From the previous chapter we now know that dark matter collapses to form halos which are the sites of galaxy formation. The next question to ask is can we model these halos with a density profile? To answer this question one may turn to N-Body cosmological simulations and attempt to derive fitting formulas for the halos that form.

It has been shown that the dark matter halos that arise in N-body simulations follow a universal density profile [43]. Universal here means that this profile is applicable to halos of all masses and redshifts. The so-called NFW[1] profile is given by;

$$\rho(r) = \frac{\rho_s}{\frac{r}{r_s}\left(1+\frac{r}{r_s}\right)^2} \tag{2.1}$$

where ρ_s and r_s are constants. Note that the profile falls of quickly for $r > r_s$, this is because all dark matter halos have a dense core and a diffuse envelope [43].

[1] Stands for Navarro Frenk and White who are the founders of the formula

2.1.2 Departure from Spherical Symmetry

It is clear that when assuming a NFW profile that the halos are considered to be spherical. Spherical symmetry is a common assumption in many branches of physics and is an excellent model for many results. But it was known from N-Body simulations, as far back as the late 1980's, that dark matter halos are actually triaxial [23]. Now in higher resolution simulations it is easy to see the halos are actually elongated and appear to be more ellipsoidal. For example Fig. 2.1 shows some snapshots of FOF halos from the simulations run for this particular project. One can see that not only are the halos ellipsoidal but they are also surrounded by a lot of substructure.

The spherically symmetric NFW profile has been extremely successful in explaining the rotation curves of galaxies, but consider a recent example of a study where a move towards a triaxial density profile is pursued to explain the discrepancy of the spherical NFW profile in Low Surface Brightness galaxies (LSBs) [26]. Note that the NFW profile is singular, whereas observations of velocities of LSBs show that the halo may have a constant density core. By simulating similar halos, the authors conclude that such effects could be produced because of the simplifying assumption of spherical symmetry when the actual halo is triaxial [26]. In another study, [38], it is found that when considering cluster lensing scenarios more accurate results are achieved if an elliptical model is used over an axially symmetric model. By ray-tracing through N-Body simulations and creating mock lensing systems the authors conclude that the inner slope of the density profile is more accurately recovered as opposed to using an axially symmetric model which underestimates the inner slope of the profile. They claim that not accounting for ellipticity in observations can lead to false conclusions against the CDM model.[38]. Recently it has also been shown that triaxiality of the halos introduce bias in SZ and X-ray measurements [13], where usually a spherically symmetric profile is assumed and the assumption is that averaging over many different projections eliminates the effects of triaxiality. The authors show that averaging may not eliminate all biases introduced by projection of triaxial halos[13]. Similarly another study [65] shows that assuming spherical symmetry when determining H_0 from SZ and X-ray observations

can lead to biases. The above only mentions some of the work that has been done in the direction of deviations from spherical symmetry. In the rest of this chapter we explore further research that strengthens these ideas.

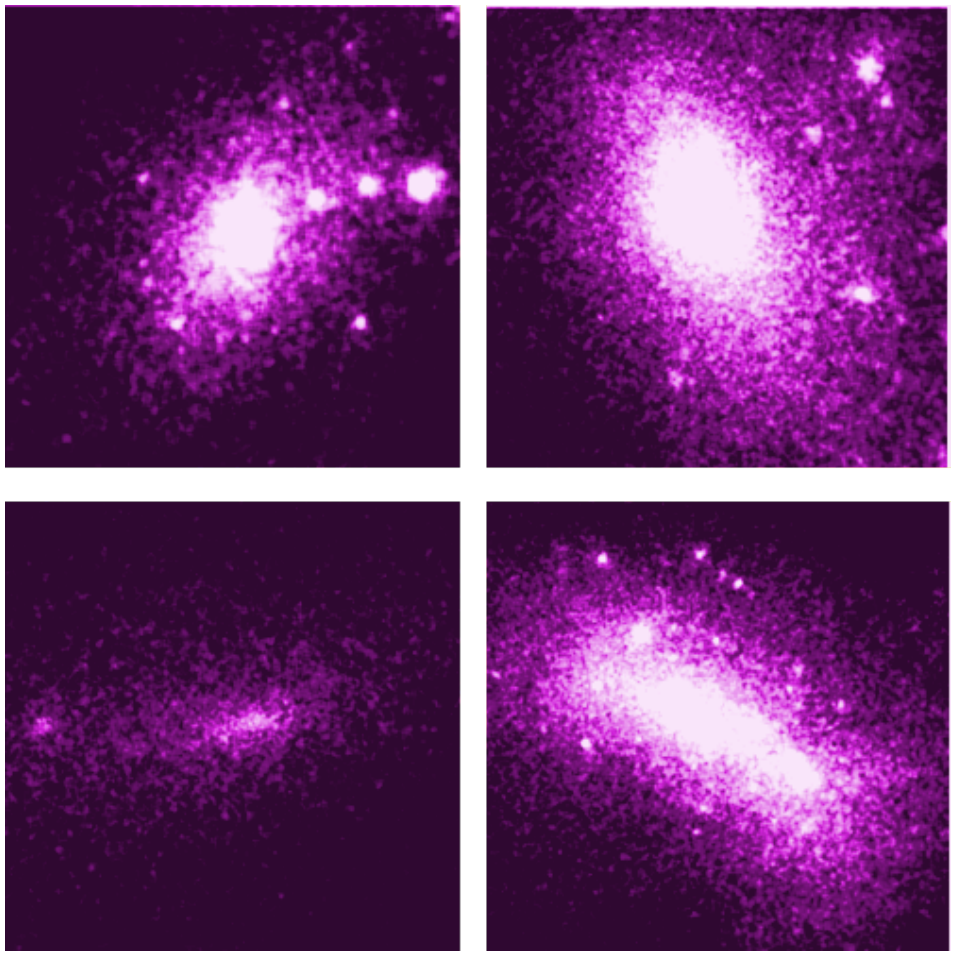

Figure 2.1: Snapshots of FOF halos at $z = 0$ from high resolution simulations, note that the halos are actually ellipsoidal

2.2 The Shape of Dark Matter Halos

2.2.1 Definitions

Before we begin our discussion of the shapes of dark matter halos it is useful to define some important quantities that will come up in this section and beyond;

- *Virial Mass* M_{200}: This is the mass of a halo contained within a radius of R_{200} which is the radius within which the mean density the halo is 200 times the critical density, $\rho(R_{200}) = 200\rho_c$.
- *Concentration* c_{200}: This is defined as R_{200}/r_s, where r_s is the scale radius of the NFW profile, E.q 2.1.
- *Sphericity* c/a: This is the ratio of the smallest axis length to the longest from 3D fitting of an ellipsoid.
- *Elongation* E: This is a parameter that tells use how elongated a halo is, $E = (b^2/a^2 + c^2/a^2)/2$.
- *Triaxiality* T: This s defined as $T = (a^2 - b^2)/(a^2 - c^2)$ where $T = 1$ means highly prolate and $T = 0$ means highly oblate.
- *Age* $z_{0.5}$: This is defined as the redshift at which the halo has grown to 50% of the mass it has at $z = 0$.
- *Age* $z_{0.2}$: This is defined as the redshift at which the halo has grown to 20% of the mass it has at $z = 0$.

2.2.2 The Moment of Inertia Tensor Method

We have seen that the dark matter halos are indeed ellipsoidal but how may one quantify the degree to which the halo is elongated? One method that is used frequently in the

literature is the moment of inertia tensor method. The moment of inertia tensor, I, is a commonly used matrix in classical physics. It carries information about an objects moment of inertia when it is rotated about arbitrary axes. Quantitatively, $\vec{L} = I\vec{\omega}$, where $\vec{L}$ is angular momentum and $\vec{\omega}$ is the angular velocity. But in the context of halos, I finds another useful purpose.

We assume that the moment of inertia tensor, I, for a halo of mass M, is equivalent to the moment of inertia tensor, I^E of a solid uniform density ellipsoid of the same mass, M. Note that aside from the mass, which sets the volume of the ellipsoid. Three other parameters are needed, a, b and c, which are the axis lengths of the ellipsoid. The aim is to solve for these three numbers for a given halo distribution. In Appendix A it is shown that if one defines the moment of inertia for a mass distribution as;

$$\tilde{I}_{ij} = \frac{1}{K} \sum_k m_k r_{k,i} r_{k,j} \tag{2.2}$$

then the eigenvalues of $\tilde{I}$ correspond to a^2, b^2 and c^2. Here $K = M/5$, $M = \sum_k m_k$ and $r_{k,i}$ and $r_{k,j}$ are the i and j components of the position $\vec{\mathbf{r}}_k$ of particle k. With these three numbers a, b and c the ellipsoidal shape of the halo is quantified. We will call the matrix, $\tilde{I}$, the second moment tensor since it bears resemblance to taking second moments.

2.2.3 A Triaxial Density Profile

In the above section a systematic way to quantify the shape of the halo was explained. In 2002, Jing & Sutto provided a detailed study of the shapes of halos in N-body Simulations, complete with a triaxial density model [31].

The method used in [31] to find halos is the FOF algorithm as described in 3.1.3, with an additional technique used to eliminate bridges; first they use a linking length of $l = 0.1\bar{d}$ to classify the halos, they claim that this does get rid of the bridges but it comes with a price, the halos that are found tend to be overdense. To remedy this, they then compute the gravitational potential of all the particles in the halo and then select the particle with the

lowest potential to be the center of the halo. They then compute the spherical overdensity of the particles with increasing radius until it reaches a certain overdensity [2].

To describe the triaxiality of the halos, the authors argue that although the moment of inertia method (MOI), as described in Section 2.2.2, is well-defined when just measuring the ellipsoidal shape of the halo, it does have some shortcomings for their particular study. They argue that the MOI method assumes in advance the membership of particles in a particular halo. A way around this is to apply the method iteratively, whereby, one starts with all the particles within a certain spherical radius and then finds the encompassing ellipsoid by applying the MOI method. Then the process is repeated by discarding particles that are outside the halo, this process is repeated until it converges. The authors find that this procedure has been successful for low resolution simulations, but for their simulations they find the method does not converge as there is a lot of resolved substructure surrounding the halo. Secondly, they claim that their aim is not just to define the shape of the halo but to build a triaxial density profile. So the method they employ instead is to find the isodensity contours for the halos. For each particle of the halo they use 32 of its closest neighbors to compute the local density of the particle by a smoothing kernel, this is similar to the technique used in this thesis as described in Section 3.2.3. After this they look for particles that fall within a small range close to 5 isodensity contours. They define the isodensity contours as $\rho_s^{(n)} = 100 \times 5^{n-1}\rho_{crit}$ where n runs from 1 to 5. The range is given by, $0.97\rho_s^{(n)} < \rho_i < 1.03\rho_s^{(n)}$, where ρ_i is the local density of the particles. Note that the authors still had to eliminate some of the tiny contours that came from substructure, they did this by once again applying the FOF procedure with varying linking lengths.

So, above we saw the method used by Jing and Suto to find the iso-density surfaces on the halos[31]. After the surfaces where found the authors applied the MOI method to the particles in the surface and fitted an ellipsoid to each surface thus obtaining the axis lengths a, b and c. The trend they found amongst all halos is summarized by the following

[2]This overdensity is given by $\rho(z)/\rho_{crit} = 18\pi^2 + 82(\Omega(z) - 1) - 39(\Omega(z) - 1)^2$

fitting formulas [31],

$$c/a = 0.56 \left(\frac{\rho_s/\rho_{crit}}{2500} \right)^{0.052} \tag{2.3}$$

and,

$$b/a = 0.71 \left(\frac{\rho_s/\rho_{crit}}{2500} \right)^{0.040} \tag{2.4}$$

where $a \geq b \geq c$. Note that these fitting formulas imply that halos are more elongated in the central regions as opposed to the outer regions which are less elongated. They also found a dependence with mass, where halos with lower mass where found to be rounder than halos of higher mass. They also considered the alignment of each of the iso-density surfaces, they found that the major axes of the each surface aligned well for about 70% of the halos. Further the authors also conducted comparisons of a triaxial density profile, with constant axis ratios, with a spherical density profile. Broadly speaking, they found that the triaxial profile was considerably better but it suffered towards the edges of the halo due to substructure. The rest of their study was devoted to constructing global probability distributions for different parameters, one should consult the actual paper [31] for more details on this and the results described above.

Consistent with Jing & Sutto 2002 [31], Allgood et al. 2005 [3] found that halos of high mass were more elongated then those of low mass and that younger halos were more elongated then older halos[3]. They also showed the dependence of halo shape with the normalization σ_8. In agreement with the arguments provided in Section 1.3.2, the relationship they found was that a high value of σ_8 resulted in halos that were more spherical than those produced by a low value of σ_8, the trend with mass and age was still maintained though.

2.2.4 Model Independent Evidence

More compelling evidence for the importance of shape parameters comes from studies done using Principal Component Analysis (PCA) and rank correlation analysis. The rank

correlation analysis is used to look for correlations between different dimensions of a data set. A commonly used technique to achieve this is by computing the Spearman Rank Correlation Coefficient ($SRCC$). Say there are two sets of data X_i, Y_i with ranks x_i, y_i, where rank just means that the data is either arranged in ascending or descending order and if two or more points have that same rank, i.e, they are equal, then an average rank is computed so that they all have the same rank. Once this is done then the $SRCC$ is given by [58];

$$SRCC = \frac{\sum_i (x_i - \bar{x})(y_i - \bar{y})}{\sum_i (x_i - \bar{x})^2 (y_i - \bar{y})^2} \tag{2.5}$$

where $\bar{x}$ and $\bar{y}$ are the mean rank. A $SRCC$ of 1 indicates that the data is strongly correlated and conversely, a $SRCC$ of -1 indicates that the data is strongly anti-correlated. A $SRCC$ of 0 indicates that the two data sets are independent. The PCA analysis on the other hand aims to reduce the dimensionality of the data. The procedure by which this is done is briefly outlined in the following.

Given a data set with k random variables,$\{X_1, X_2 ... X_k\}$, one can compute the covariance matrix [58];

$$C_{ij} = \mathrm{E}\left[(X_i - \mu_i)(X_j - \mu_j)\right] \tag{2.6}$$

where $\mathrm{E}[X]$ is the operator for the mean, and $\mu_i = \mathrm{E}[X_i]$. One can standardize this data so that each random variable has mean 0 and then compute the eigenvectors and eigenvalues of the resultant covariance matrix. These eigenvectors are know as the principal components, $\{PC_1, PC_2, ..., PC_k\}$. The eigenvalues corresponding to these principal components tell us how much a particular PC_i contributes to the total variance in the data set. This can help reduce the dimensionality from k if PC_i's with a low eigenvalue are dropped. Or put in another way, PC_i's with a high eigenvalue are considered to be more fundamental. To find which of the original random variables, $\{X_1, X_2 ... X_k\}$, a particular PC_i is closest to one can compute the $SRCC$'s and see which random variables correlate the strongest with the PC_i. Note that the above methods look for correlations between different parameters of the halo free of any parameters, i.e., there is no representative model used. This makes

this a very powerful technique in uncovering underlying patterns as there are very few assumptions put in.

Coming back to the topic at hand, in what follows we discuss some recent studies that have applied PCA and rank correlation techniques to halo parameters. These studies include Wong & Taylor 2012 [71], A. Jeeson-Daniel et. al. 2011 [29], and Skibba & Maccio 2011 [60], we will call these WT12, JD11 and SM11, respectively. The basic idea was to compute different halo parameters and compute correlations and PC_i's. WT12 used a sample of 4672 halos from 3 simulations with box sizes 60, 120 and 240 Mpc/h and 512^3 particles. JD11 constructed their halo sample from 5 simulations with box sizes from 25 Mpc/h to 400 Mpc/h, increasing by factors of two. Each simulation had 512^3 particles and the final sample had 1867 particles. SM11, on the other hand, ran 8 different simulations with box sizes in the range of 20 - 300 Mpc/h and particle counts in the range of 250^3 - 400^3, the exact details can be found in [60].

WT12's work shows how halo parameters relate to the formation history of the halo. In the first part of their study they explore the Mass Accretion Histories of the halos (MAHs), which is simply the ratio of the mass at a certain redshift to the final mass of the halo at redshift 0, i.e, $M(z)/M(0)$. Usually the MAH is fit by a formula that depends on two parameters, but WT12 argue that it may be possible to reduce this to one parameter. By doing a PCA analysis of the MAHs of 817 halos they conclude that the vector with the most variance (60%), PC_1, corresponds to the age of the halo. Motivated by this, they provide a new single parameter formula for the MAHs.

Further, using the SRCC, WT12 consider how the different halo properties (some of these are mentioned in Section 2.2.1, for a full list please consult [71]) correlate which each other. They found that concentration was strongly linked with age indicators, like $z_{0.5}$. The also found that the shape indicator, E (elongation), was linked to concentration. The authors also conducted a PCA analysis to see which halo properties caused the most variance in the data, this is similar to their treatment for the MAHs as described above. The vector with the highest variance, PC_1, correlated strongly with age indicators ($z_{0.5}$

and $z_{0.2}$), and concentration. This makes sense as concentration is strongly linked with age. There was also significant contribution to PC_1 from mass and elongation, although not as strong as age and concentration. But WT12 found that shape parameters correlated strongly with PC_2, more than that with PC_1 which suggested that there was another parameter that affected shape aside from age.

Since shape is correlated with age and hence formation history, WT12 aim to explore this. They consider the possibility that the final shape of the halo is somehow related to the shape of the initial matter distribution that collapsed to form the halo. To check this they measure the shape of the halo at earlier redshifts and compare it to the final shape of the halo. They conclude that the shape of the halo is correlated with recent redshifts, $z < 1$, but not higher, this suggests that the shape of the halo maybe conserved as the halo accretes mass, but is not conserved with the initial mass distribution from which the halo forms.

The analysis done by JD11 shows results that are not to far off from WT12. Their main focus was on the halo properties and not on the formation history of the halo. They too found that concentration was strongly linked with age, where the age indicator that they use is $z_{0.5}$. Further they also find that shape and mass are correlated with concentration. Do note that the shape indicator that JD11 use is sphericity, c/a. They also do a PCA analysis, where they find that PC_1 is *very* strongly (SRCC $= -0.86$), correlated with concentration. They also find that the shape parameter of triaxiality is significantly correlated with PC_1. The share of the variance for PC_1 was 37%. They conclude, again similar to WT12, that concentration, age, mass and shape are quite intertwined and likely belong to a single family of parameters. As for SM11 they did not provide correlations between different halo parameters but their PCA analysis concluded that concentration was highly correlated with PC_1.

2.2.5 Taking a Step Back

In this chapter we discussed some interesting results that aim to show the importance of halo triaxiality. We began by mentioning how the assumption of spherical symmetry breaks down under certain conditions. Then we discussed some steps that can be taken to classify and quantify the triaxiality of the halo, i.e, the MOI method and the triaxial density profile introduced by [31]. Finally, we discussed some recent studies that show some very interesting trends in between halo properties. To summarize some general trends,

- We saw that age of the halo was a fundamental parameter for halo properties. It was strongly linked with the formation history of the halo through the MAHs such that it was possible to construct a fitting formula for the MAHs based on age alone [71].
- Age indicators such as $z_{0.5}$ were strongly linked to the concentration. Older halos (higher $z_{0.5}$) are found to be more concentrated.
- Mass is linked to both concentration and age. Older halos were less massive then younger ones. More massive halos were less concentrated. This suggests that halos that have formed from mergers are massive and hence less concentrated. This likely due to the cores being disturbed during mergers. Note also that massive halos formed from major mergers happen later and thus are younger.
- Shape and concentration are linked, more concentrated halos were rounder. Together with the link between age and concentration, this result ties in together nicely with the argument that older halos are more relaxed and thus rounder.

There are of course more trends, but the above pointers are useful for the purposes of this thesis specially to test for cosmological parameters like Ω_M and σ_8 through the physics described in Section 1.3.2. Note their are numerous other studies with similar results, [8] [33] [24] [32] to name a few.

2.2.6 Effect of Baryons on Halo Shape

So far, in Sections 2.2.3 and 2.2.4, we have seen the treatment for halo shapes without including the effect of baryonic physics. The main cause for this is the increased computational resources required to add the complex hydrodynamics of baryons. But work has been done in this direction; an example is the work done by Kazantzidis et. al. 2004, [34]. Here, the authors studied the gas dynamics in eight group-sized systems and one galaxy-sized system. To achieve this they conducted cosmological simulations with the Adaptive Refinement Tree N-Body + gasdynamics code developed by Kravtsov et. al. [36]. They explored the effects on halo shape by radiative cooling, first by including gas dynamics that is adiabatic and then comparing that with the same simulation now run with other baryonic effects included, for e.g., star formation, metal enrichment, metallicity and density dependent cooling, feedback, etc. Broadly speaking, they found that the adiabatic simulations produced results very close to the pure dark matter simulations and the latter showed halos that were more spherical. They found the effect to be more pronounced in the center, decreasing with radius, but still significant at the virial radius. On average the axis ratios increased by a factor of $\sim$ 0.2 - 0.4 in the central regions of the halos. The authors explain that due to cooling the baryons at the center condense which in turn changes the gravitational potential. The dark matter particles respond to this change in potential and move towards the center creating a more concentrated dark matter halo [34]. In earlier work, Dubinski 1994 showed that having a denser core modifies the orbits of the particles in a manner such that the halo evolves towards a more spherical shape[19]. There has also been more recent work on this topic; Bryan et. al. 2012 [12] did a comprehensive study using data from the OWLS simulations. Where OWLS stands for OverWhelmingly Large Simulation. They used data from 9 different kinds of simulations (please see [12]) and found, consistent with the results mentioned above, that baryonic effects make halos more spherical. If the results of this thesis are used to test with observational data then these baryonic effects would have to be taken into account some way.

2.3 Gravitational Lensing

In Section 1.3.2 and Section 2.2 we discussed how the shape of dark matter halos could be a useful probe of cosmological parameters. But an important question to ask is, can the shape of halos be experimentally measured by any observational techniques? One candidate for such a technique is gravitational lensing. The following brief treatment of some of the formalism of lensing closely follows [7].

Like any ordinary lens, gravitational lenses work by the bending of light rays. In an ordinary lens the bending of light is caused by the changes in the refractive index of the medium the light is traveling in. In the case of gravitational lenses the bending is caused by the curvature of space-time itself around a massive body. If we consider this massive body to be a point mass then the light ray is deflected by an angle given by;

$$\alpha = \frac{4GM/c^2}{\xi} \tag{2.7}$$

where ξ is the impact parameter, as can be seen in Fig. 2.2. We can extend this same idea to a mass distribution rather than just a point mass. In that case the angle of deflection is given by;

$$\vec{\alpha}(\vec{\xi}) = \frac{4G}{c^2}\int d^2\xi' \Sigma(\vec{\xi'})\frac{\vec{\xi}-\vec{\xi'}}{|\vec{\xi}-\vec{\xi'}|^2} \tag{2.8}$$

where $\Sigma(\vec{\xi'})$ is the surface mass density of the lens plane and $\vec{\xi'}$ is the 2-dimensional vector for the lens plane. In the above equation we have made the assumption of thin lensing planes. This means that the lengths D_d and D_{ds} are large as compared to the length scale of the mass distribution. From the geometry of the lens we can construct the following lens equation;

$$\vec{\beta} = \vec{\theta} - \frac{D_{ds}}{D_s}\vec{\alpha}(D_d\vec{\theta}) = \vec{\theta} - \vec{\tilde{\alpha}}(\vec{\theta}) \tag{2.9}$$

where $\vec{\eta} = D_s\vec{\beta}$, $\vec{\xi} = D_d\vec{\theta}$ and the scaled deflection angle, $\vec{\tilde{\alpha}} = \frac{D_{ds}}{D_s}\vec{\alpha}(D_d\vec{\theta})$. Essentially Eq. 2.9 is a coordinate transformation for the coordinates of the source plane. When a lensing plane is not present sources have coordinates $\vec{\beta}$ and when it is present, and light rays are deflected, the same sources now have coordinates $\vec{\theta}$.

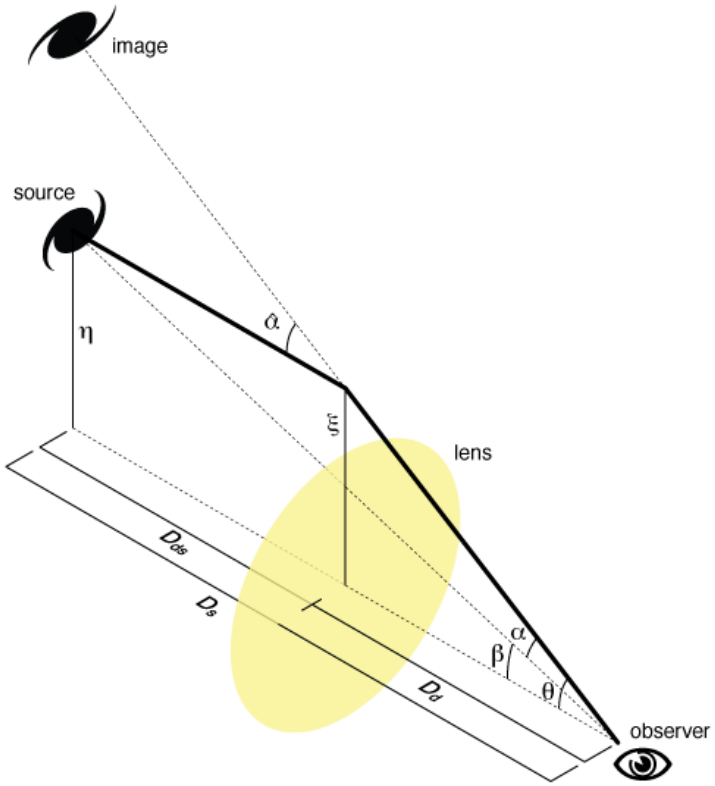

Figure 2.2: A typical lensing scenario [68]

In Eq. 2.9, there could be more than one solution for $\vec{\theta}$ for a given $\vec{\beta}$. Clearly this is determined by what form $\vec{\tilde{\alpha}}$ has as a function of $\vec{\theta}$. We can classify some solutions if we express $\vec{\tilde{\alpha}}$ as;

$$\vec{\tilde{\alpha}}(\vec{\theta}) = \frac{1}{\pi}\int d^2\theta' \kappa(\vec{\theta'}) \frac{\vec{\theta} - \vec{\theta'}}{|\vec{\theta} - \vec{\theta'}|^2} \tag{2.10}$$

where a new quantity, $\kappa(\vec{\theta})$, called the convergence has been introduced. It is given by

$$\kappa(\vec{\theta}) = \frac{\Sigma(D_d\vec{\theta})}{\Sigma_{cr}} \tag{2.11}$$

where Σ_{cr} is a critical density given by;

$$\Sigma_{cr} = \frac{c^2}{4\pi G}\frac{D_s}{D_d D_{ds}} \tag{2.12}$$

If $\kappa \geq 1$ then this is a sufficient condition for producing multiple images, and is called strong lensing. If $\kappa < 1$ this may or may not produce multiple images, this regime is called weak lensing. In this thesis, we will focus mainly on weak lensing and how this can be used to measure shapes of halos.

The field of weak lensing is rich and its treatment would require a thesis in itself. But the basic idea is rather simple. One can study the slight distortions of the shapes of distant galaxies to construct the mass distribution in the lensing plane. But there is an obstacle in the way of this approach, galaxies are not exactly circular, but rather have an intrinsic ellipticity.

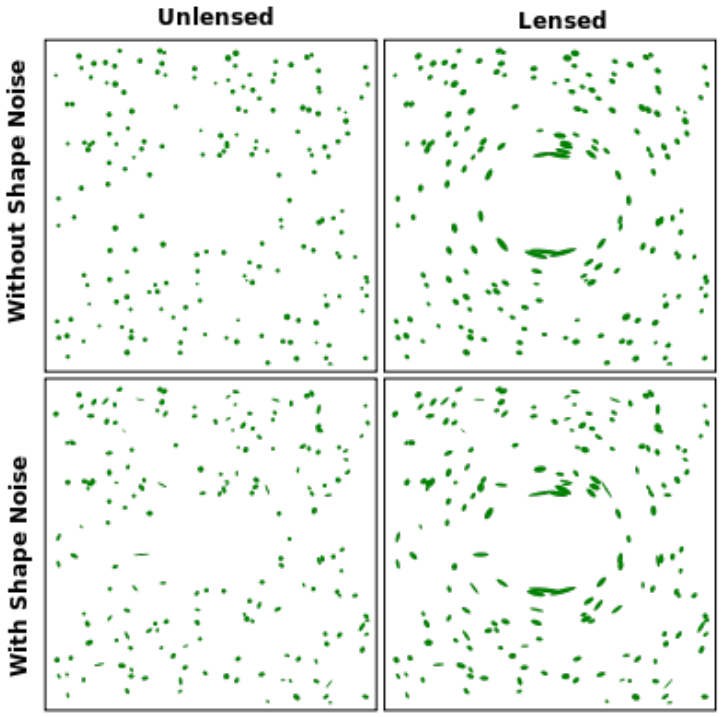

Figure 2.3: The above illustration demonstrates the effect of the intrinsic ellipticity of background galaxies and how they introduce shape noise. Not only are they elliptical but they are also randomly oriented [69].

As can be seen in the above figure, if the galaxies are assumed to be circular they tend to get distorted in a manner that makes them appear elliptical. One could simply measure how elliptical each galaxy is and the mass distribution could be constructed. But, in reality the case is similar to the bottom two panels. Galaxies have their own ellipticities and are randomly oriented. This introduces a *shape noise*, and the mass distribution can only be constructed if the local net ellipticity of a sample of galaxies can exceed this noise [7].

2.3.1 Can Weak Lensing Measure Halo Shape?

As we have seen previously, the knowledge of the halo's shape can help make useful predictions. Oguri et al. 2010 made ellipticity measurements of X-ray luminous clusters by using the 2-dimensional signals obtained from the Subaru/Suprime-Cam data [48]. The method employed by Oguri et al. 2010 involved doing χ^2-fits of the 2-dimensional elliptical NFW-profile to the mass maps created from shear profiles. In doing these fits two sources of error were added by making use of a covariance matrix. As mentioned in the previous section, one source of error was the shape noise from the background galaxies used to determine the shear and the other source of error was from the mass in between the observer and the cluster. The gravitational lensing effect caused by this mass along the line of sight is called *cosmic shear*. It can be predicted and accounted for analytically from the power spectrum $P(k)$ for a given set of cosmological parameters, in this case the ΛCDM. Note that Oguri et al 2010 do not account for the error introduced by substructure close to the halo, as they claim that it is negligible over the angular scales they considered [48].

The 2-dimensional profile used was the NFW profile in projection which is given by [6];

$$\Sigma(x) = \frac{2\rho_S r_s}{\xi^2 - 1} f(\xi) \tag{2.13}$$

where $\xi = r/r_s$ and;

$$f(\xi) = \begin{cases} 1 - \frac{2}{\sqrt{\xi^2-1}} arctan\sqrt{\frac{\xi-1}{\xi+1}}, & (\xi > 1) \\ 1 - \frac{2}{\sqrt{1-\xi^2}} arctanh\sqrt{\frac{1-\xi}{1+\xi}}, & (\xi < 1) \\ 0, & (\xi = 1) \end{cases} \tag{2.14}$$

This was then made elliptical in the following way [48];

$$\xi^2 = \left[\frac{x'^2}{1-e} + (1-e)y'^2\right]\frac{1}{r_s^2}, \tag{2.15}$$

where $e = 1 - b/a$ is the ellipticity and a and b are the major and minor axes. Note further that,

$$x' = x\cos\theta_e + y\sin\theta_e \tag{2.16}$$

$$y' = -x\sin\theta_e + y\cos\theta_e \tag{2.17}$$

where θ_e is the orientation of the halo. Now the 2-dimensional profile is characterized by six parameters $\{\rho_s, r_s, e, \theta_e, x_c, y_c\}$, where x_c and y_c is the center of the halo. These six parameters are the ones that were fitted using the χ^2-fit [48]. With the ellipticity being the one of main interest. From a sample of 18 clusters they found the mean ellipticity to be;

$$\langle e \rangle = \left\langle 1 - \frac{b}{a} \right\rangle = 0.46 \pm 0.04(1\sigma) \tag{2.18}$$

In 2012, another paper was published by Oguri el. al. 2012 [47]. In this study a combined analysis of strong and weak lensing was made from a sample of 28 galaxy clusters. The clusters were selected from their strong lensing signal from Sloan Giant Arcs Survey and weak lensing measurements were made from the deep Subaru/Suprime-cam images. This study, however, was focused more on concentration measurements. Their findings concluded the following relationship between concentration and mass for halos with high mass, $\sim 10^{15}h^{-1}M_\odot$;

$$c_{vir} \propto M_{vir}^{0.59\pm0.12} \tag{2.19}$$

However, for low mass halos they concluded their estimates were overestimated. As for the shape measurements, a stacked analysis was performed. The position angle information was used from the strong lensing measurements. The average ellipticity found through this method was,

$$\langle e \rangle = \left\langle 1 - \frac{b}{a} \right\rangle = 0.47 \pm 0.06 \tag{2.20}$$

which is almost the same as their previous measurements, Eq. 2.18. Our aim is to explore this method of measuring shape. The next Chapter is devoted to this.

Chapter 3

Methodology and Results

3.1 N-Body Simulations

The predictions made by evolving the density field are achieved from using linear perturbation theory as the equations of motion used are non-linear [50]. To solve them exactly, one has to resort to N-Body methods. As the name suggests, the approximation is that the density field is represented by a set of N discrete particles. At the fundamental level the idea is quite simple: in a finite volume, for every particle calculate the gravitational attraction caused by all the other particles and then update the position of the particle based on the gravitational acceleration. In the work carried out for this thesis the code used was GADGET-2 [62].

3.1.1 Softening Length

Since our focus is only on dark matter the physics involved has collisionless dynamics. We are dealing with particles and they can get arbitrarily close to each other and this can lead to unrealistically high accelerations. To combat this problem GADGET-2 uses a softening

spline kernel with a smoothing length of ϵ [62]. The result of this is that the potential of each particle is modified such that as $r \to 0$ the potential is finite at $-GM/\epsilon$.

3.1.2 Trees and Meshes

GADGET-2 combines two techniques to compute the force on each particle. One is the Tree Method, which involves recursively splitting a cube of space into eight daughter nodes, until the final nodes (or leaf nodes) contain only one particle. Once the tree is constructed then a decision can be made whether or not to open a node based on the accuracy of the force required. The other technique is the Particle Mesh Method, which involves splitting the volume into cells and computing the density of each cell. The gravitational forces are then computed by solving the gravitational Poisson equation for the potential. GADGET-2 allows for different configurations of these two methods. The scheme chosen for this research is that Tree methods are used for short range forces and Particle Mesh methods are used for long range forces [62].

3.1.3 Halo Finding

As discussed in earlier sections, dark matter clumps together to form halos. In the context of N-Body simulations a scheme is needed to locate these halos. The algorithm we use is called Friends-of-Friends (FOF). The exact software used was taken from [44]. The algorithm works in the following manner; a given particle is linked to its neighbors, or friends, based on a linking length, l, i.e., the neighbor has to be within a radius l of the given particle to be linked. Then the same is done for all other particles. The result is that dense regions which contain more particles close together get linked into one group or halo.

3.1.4 Simulations

Three simulations were run for the work involved in this thesis. One (Simulation 2) was with the latest WMAP-7 [70] results and two others with slightly different values for σ_8 and Ω_M. The parameters of the simulation are summarized in the following table;

Simulation	1	2	3
N	512^3	512^3	512^3
Box Size	120 Mpc/h	120 Mpc/h	120 Mpc/h
$\Omega_{\Lambda,0}$	0.800	0.7274	0.650
$\Omega_{DM,0}$	0.200	0.2726	0.350
σ_8	0.900	0.809	0.720
ϵ (Mpc/h)	0.00469	0.00469	0.00469
l (Mpc/h)	0.0469	0.0469	0.0469

Table 3.1: Parameters for the simulations

Note that here N, ϵ and l, are the number of particles, softening length and linking length respectively. The value of the linking length was calculated using, $l = 0.2 \times \bar{d}$, where $\bar{d}$ is the mean inter-particle separation, i.e. $\bar{d} = 120/512$.

3.2 Method

As we have seen above Oguri et al. 2010 measured ellipticity of clusters by doing a χ^2-fit of a projected 2-dimensional elliptical NFW profile on the shear maps obtained from the lensing studies [48]. Our aim in this section is to explore this technique of measuring the shape.

3.2.1 χ^2-fitting

To perform a χ^2-fit of a given data set with a model that is representative of the data one has to compute χ^2;

$$\chi^2 = \sum_i^N \frac{[M(x_i : \mathbf{P_k}) - D(x_i)]^2}{\sigma_i^2} \tag{3.1}$$

where $D(x_i)$ is your data set, $M(x_i : \mathbf{P_k})$ is a model that depends on a set of parameters $\mathbf{P_k} = \{P_1, P_2, ..., P_k\}$ and σ_i is the uncertainty for each data point. To find the parameters that best describe the model one solves the following set of equations,

$$\frac{\partial \chi^2}{\partial P_j} = 0 \tag{3.2}$$

for $j = 1, .., k$.

3.2.2 Method For 2d and 3d Shape Measurements

As stated earlier we find the halos using the FOF algorithm which gives us a halo catalog i.e., a halo ID and the corresponding particles that end up in that halo. For the 3d shape of the halo the procedure is simple. On calculates the matrix given in E.q 2.2 and finds the eigenvalues which are a^2, b^2 and c^2.

For the 2d shape, we project each halo along a randomly chosen line of sight. We then bin the resulting 2-dimensional halo particles into a grid with 64×64 cells and perform a χ^2-fit . From E.q 2.13 we saw that the model we are trying to fit depends on 6 parameters, $\{\rho_s, r_s, e, \theta_e, x_c, y_c\}$. To save computational time we use the coordinates of the center of mass of the halo for x_c and y_c which reduces our set of parameters to four, $\{\rho_s^{FOF}, r_s^{FOF}, e^{FOF}, \theta_e^{FOF}\}$, where the FOF signifies that the parameters are fitted to the FOF halo. The χ^2 is then given by;

$$\chi^2 = \sum_{i=1}^{i=64} \sum_{j=1}^{j=64} \left[\frac{\Sigma_{FOF}(x_i, y_j) - \Sigma(x_i, y_j; \{\rho_s^{FOF}, r_s^{FOF}, e^{FOF}, \theta_e^{FOF}\})}{\sqrt{N_{ij}}} \right]^2 \tag{3.3}$$

where $\Sigma_{FOF}(x_i, y_j)$ is the binned data, $\Sigma(x_i, y_j; \{\rho_s^{FOF}, r_s^{FOF}, e^{FOF}, \theta_e^{FOF}\})$ is the model from E.q 2.13 and N_{ij} is the number of particles in each bin. Note that for the uncertainty we have used the Poisson error, $\sqrt{N_{ij}}$. We sample 32 different values for the three parameters other than ρ_s which can be found analytically by solving $\partial\chi^2/\partial\rho_s = 0$. For the ellipticity we sample values in the range $0 \leq e \leq 1$ equally spaced by intervals of $1/32$. For the orientation angle θ_e we use 32 equally spaced values in the range $0 \leq \theta_e < \pi$. Note that due to symmetry this range covers all possible orientation angles. For r_s we use 32 equally spaced values in log space ranging from 0.001 Mpc/h to 2.0 Mpc/h. The χ^2 value for all possible models was computed, i.e. $32 \times 32 \times 32$ and the set of parameters corresponding to the minimum value was chosen as the best fit. Note that cells with no particles in them were not included in the χ^2 sum and to save computational time all possible models were stored in a binary file and then read as needed.

To model the effect of mass along the line of sight and substructure close to the halo the following procedure is applied. First a coordinate transformation is performed so that the center of mass of the halo is at the center of the box. This is done simply so that a line of sight can be chosen that is atleast as long as the box size. Then all particles within boxes of varying size are projected and binned into a grid of size 64×64 cells. The dimensions (in Mpc/h) of the boxes chosen are $8 \times 8 \times 2L$, $5 \times 5 \times 2L$ and $3 \times 3 \times 2L$. Note of course, that this grid is perpendicular to the line of sight which runs through the center of the box. The length of the box is written as $2L$ to signify that there is length L ahead of the halo and length L behind the halo. To get the ellipticity, the same procedure as Eq. 3.3 is applied. The best-fit parameters derived in this case are labeled, $\{\rho_s^{BOX}, r_s^{BOX}, e^{BOX}, \theta_e^{BOX}\}$.

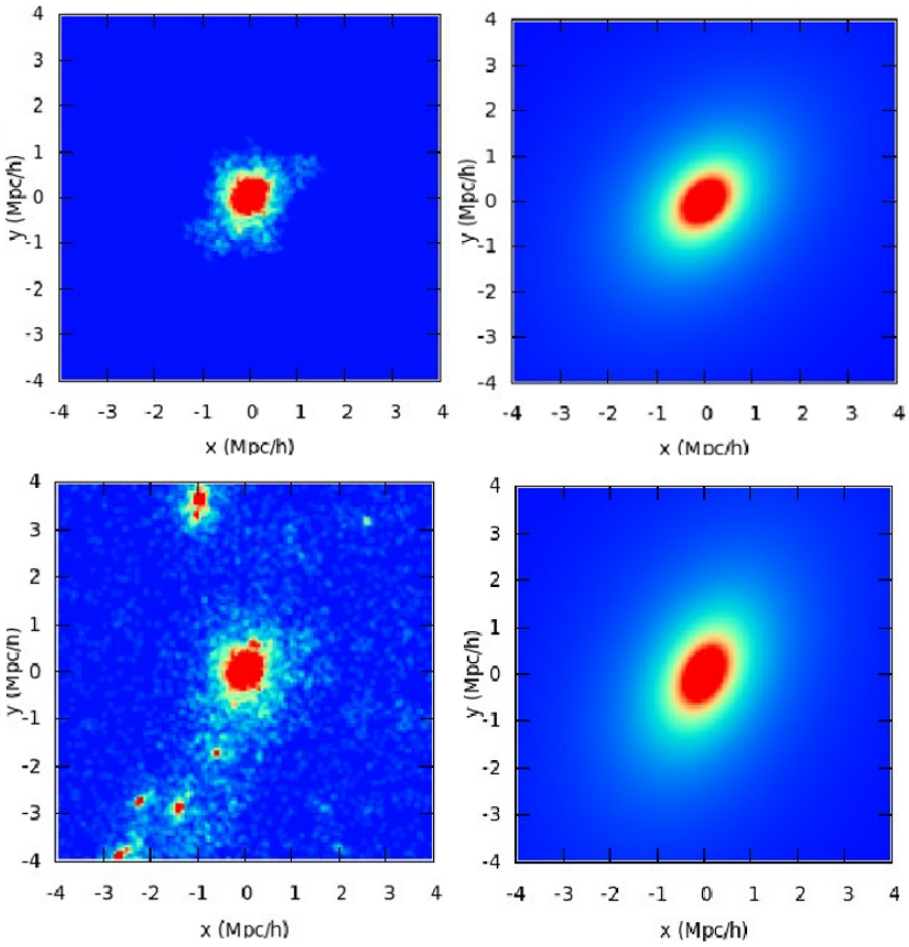

Figure 3.1: This is an illustration of the χ^2-fit , the top left panel shows just the FOF halo and the top right panel shows the fit. The bottom left panel shows the same halo but now the contribution from surrounding material is addded. The bottom right panel shows the fit. Note that both the ellipticity and orientation angle have changed slightly. This image was generated with 128 $\times$ 128 bins for illustrative purposes.

The above figure is an illustration of the procedure described above. In the top left panel we see just the halo particles projected along a line of sight and on the top right panel we see the fit for this. The bottom two panels show the halo with mass along the

line sight added and the corresponding fit. Note that this was done with 128×128 cells for illustrative purposes.

3.2.3 Method for Fitting NFW-Profile

Each halo was also fitted with a NFW profile, Eq. 2.1. This was again done using χ^2-fit . The value of χ^2 used was;

$$\chi^2 = \sum_{i=1}^{128} [\log \rho_{NFW}(r_i) - \log \rho_D(r_i)]^2 \tag{3.4}$$

where $\rho_{NFW}(r_i)$ is the NFW model and $\rho_D(r_i)$ is the radially binned data. The binning was done in the range $0.005R_{vir} \leq r \leq 0.7R_{vir}$. These values were chosen by trial and error to reduce effects of substructure at the edges of the halo and lowering the effects of reduced resolution at the center. The logarithms are used to give equal weighting to particles near the edge and particles near the center [71]. Note that the center of the halo was chosen to be the particle with the highest local density rather than the center of mass, the software SMOOTH was used to find the local density [44].

3.3 Results

This section simply lists the results obtained. Discussions are in the next chapter.

3.3.1 Effect of Large Scale Structure Along the Line of Sight

As discussed in the previous section, one of our aims is to explore the effects of Large Scale Structure (LSS) on shape measurements. Following are three plots of e_{BOX} vs. e_{FOF} for a box with dimensions 4 Mpc/h $\times$ 4 Mpc/h $\times$ $2L$ with L = 4 Mpc/h, 36 Mpc/h & 60 Mpc/h. For each value of L, 150 random lines of sights were chosen and this was done for

the top 50 (in particle number) halos from Simulation 2 . This gives us 7500 points for each L. Note that in all plots the e_{BOX} data has been binned into bins of length 1/32 in the e_{FOF} axis. The points plotted are the mean of the data in a bin and error bars show 1σ deviations.

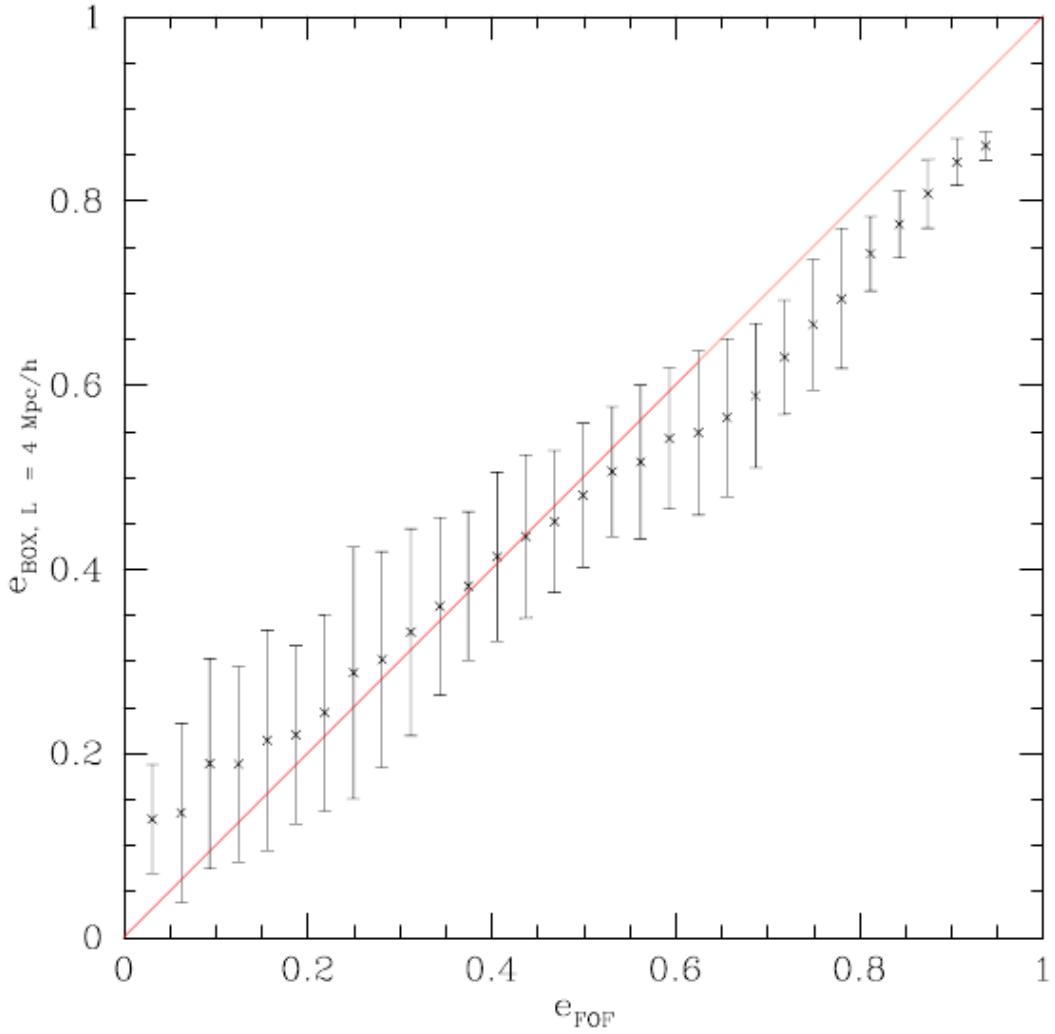

Figure 3.2: This plot shows the scatter in the ellipticity measurement when mass in a box around the halo is included. The box size for plot is $L = 4$ Mpc/h. Here e_{FOF} is the ellipticity measurement on just the FOF halo and e_{BOX} is the ellipticity measurement made after including mass along the line of sight. Note that there is a bias, spherical halos appear to be slightly elliptical and elliptical halos appear to be slightly spherical. The error bars show the 1σ deviations and the plot was made with 50 halos $\times$ 150 lines of sight = 7500 points.

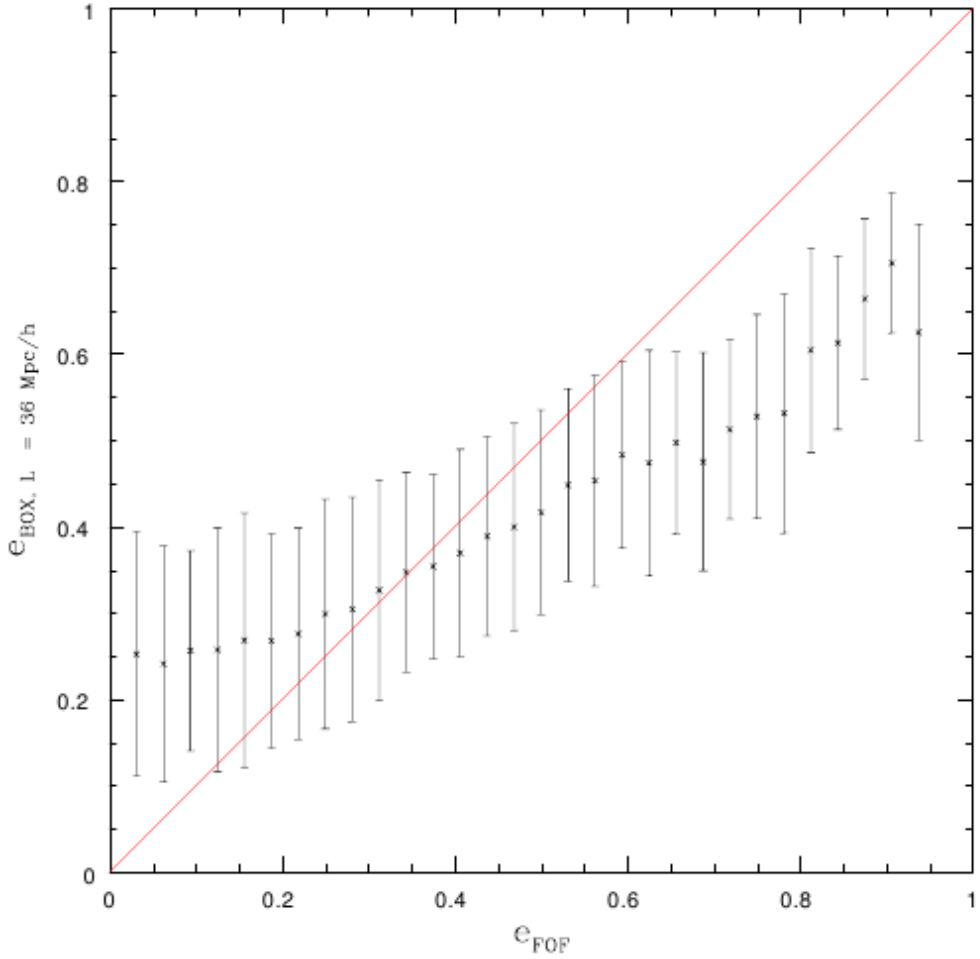

Figure 3.3: This plot shows the scatter in the ellipticity measurement when mass in a box around the halo is included. The box size for plot is $L = 36$ Mpc/h. Here e_{FOF} is the ellipticity measurement on just the FOF halo and e_{BOX} is the ellipticity measurement made after including mass along the line of sight. Note that in addition to the bias mentioned above, halos appear to be more spherical overall. The error bars show the 1σ deviations and the plot was made with 50 halos $\times$ 150 lines of sight = 7500 points.

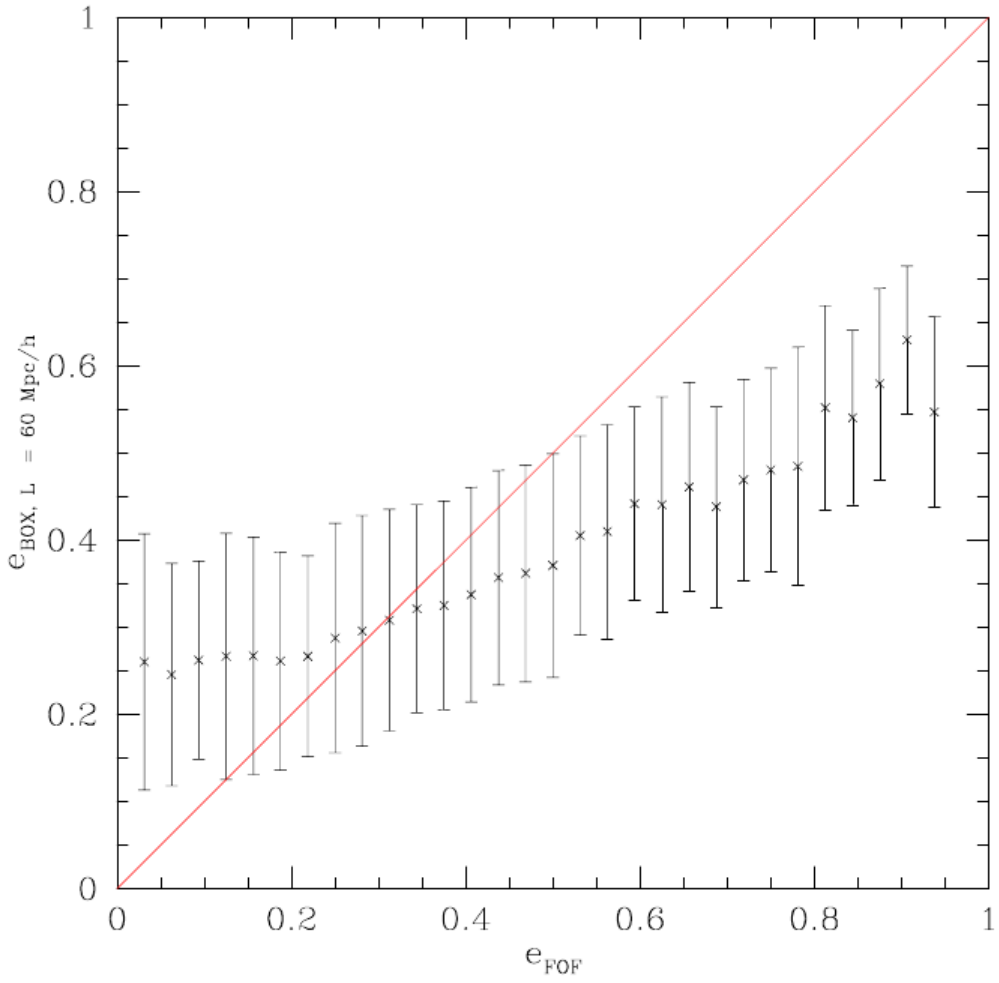

Figure 3.4: This plot shows the scatter in the ellipticity measurement when mass in a box around the halo is included. The box size for plot is $L = 60$ Mpc/h. Here e_{FOF} is the ellipticity measurement on just the FOF halo and e_{BOX} is the ellipticity measurement made after including mass along the line of sight. Note that in addition to the bias mentioned above, halos appear to be more spherical overall even more so then in Fig. 3.3. The error bars show the 1σ deviations and the plot was made with 50 halos $\times$ 150 lines of sight = 7500 points.

Since there is a clear deviation from $e_{BOX} = e_{FOF}$ which increases for different L. It is informative to plot $e_{BOX} - e_{FOF}$ Vs. e_{FOF} for each L. The following Figs. 3.5, 3.6 and 3.7 provide scatter plots for $e_{BOX} - e_{FOF}$ Vs. e_{FOF}. The actual scatter of the points is binned in hexagons where the color of each hexagon specifies how many points are in it with the coloring scheme given at the far right, for example red is the highest number and blue is the lowest. The distribution of the $e_{BOX} - e_{FOF}$ values is also given as a histogram in blue to the right.

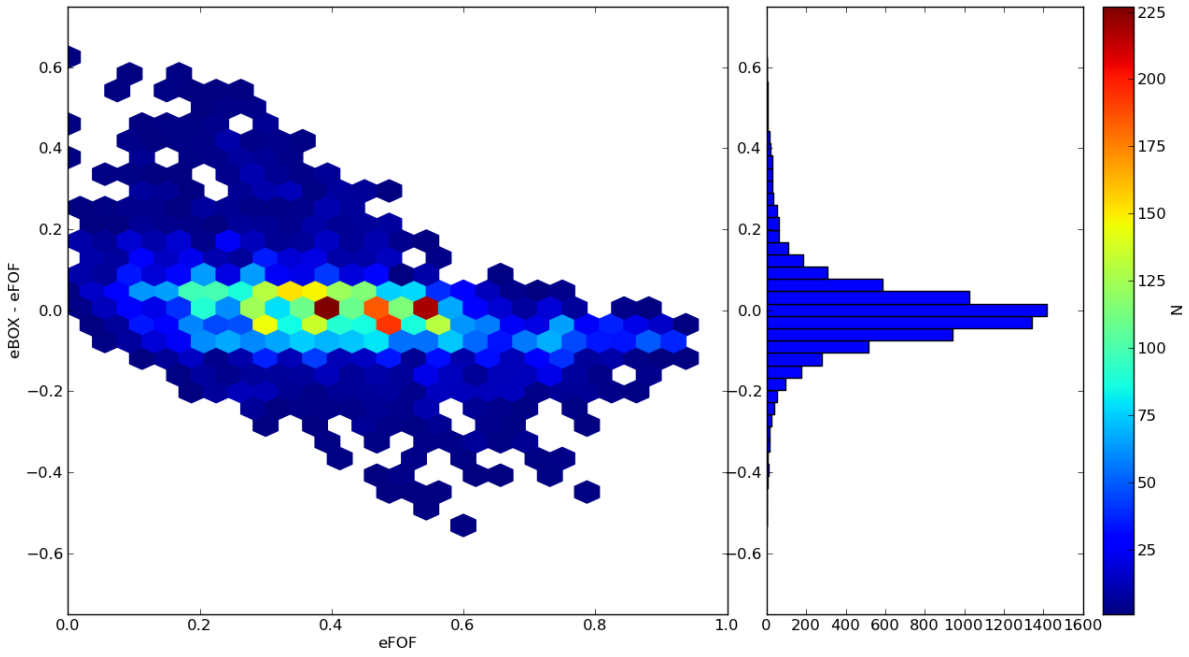

Figure 3.5: This plot is made from the same data as in Fig. 3.2, but here we show the scatter in the difference $e_{BOX} - e_{FOF}$. The plot in the right panel is a histogram of the $e_{BOX} - e_{FOF}$ values.

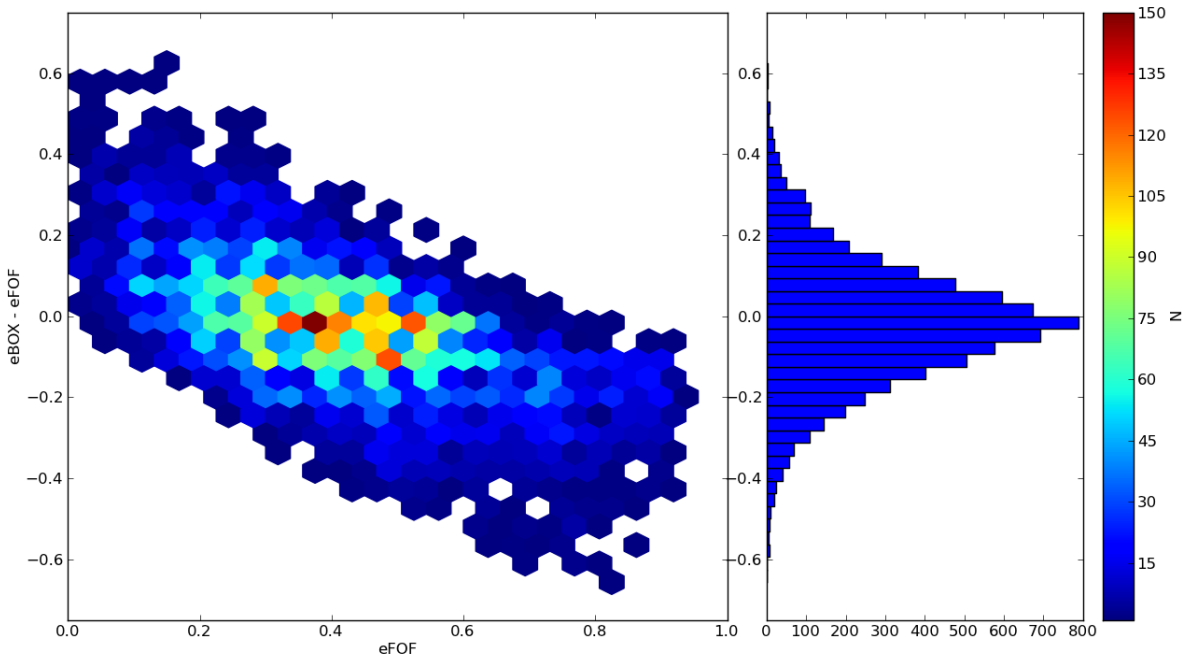

Figure 3.6: This plot is made from the same data as in Fig. 3.3, but here we show the scatter in the difference $e_{BOX} - e_{FOF}$. The plot in the right panel is a histogram of the $e_{BOX} - e_{FOF}$ values.

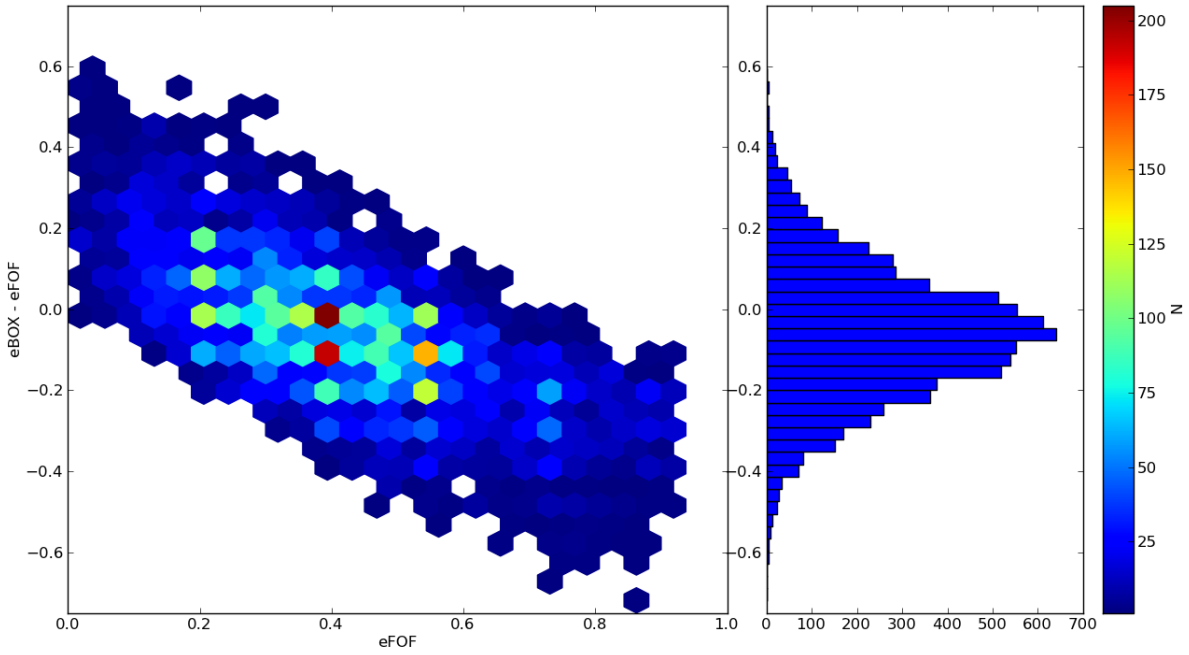

Figure 3.7: This plot is made from the same data as in Fig. 3.4, but here we show the scatter in the difference $e_{BOX} - e_{FOF}$. The plot in the right panel is a histogram of the $e_{BOX} - e_{FOF}$ values. Note how the peak is < 0 showing that halos appear more spherical.

We apply the same procedure as above to different dimensions of the box. Following are three plots of e_{BOX} vs. e_{FOF} for $L = 4$ Mpc/h, 36 Mpc/h & 60 Mpc/h. But now the dimensions of the box are $5 \times 5 \times 2L$. Again, for each value of L, 150 random lines of sights were chosen and this was done for the top 50 (in particle number) halos from Simulation 2 . This gives us 7500 points for each L. Note that in all plots the e_{BOX} data has been binned into bins of length 1/32 in the e_{FOF} axis. The points plotted are the mean of the data in a bin and error bars show 1σ deviations.

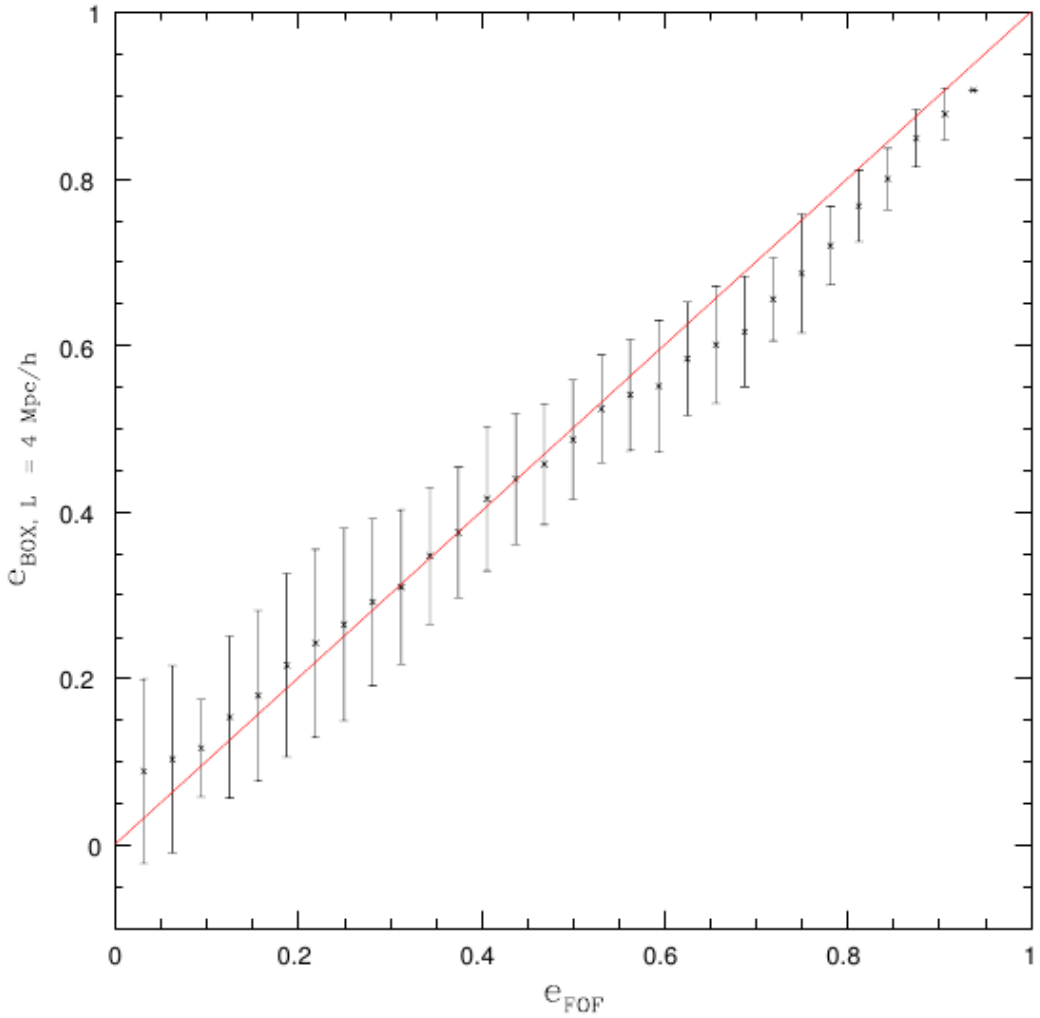

Figure 3.8: This plot shows the scatter in the ellipticity measurement when mass in a box around the halo is included. The box size for plot is $L = 4$ Mpc/h. Note that the window size is now 5 Mpc/h $\times$ 5 Mpc/h. Here e_{FOF} is the ellipticity measurement on just the FOF halo and e_{BOX} is the ellipticity measurement made after including mass along the line of sight. Note that the bias, from Fig 3.2, of spherical halos appearing to be slightly elliptical and elliptical halos appearing to be slightly spherical is reduced considerably. The error bars show the 1σ deviations and the plot was made with 50 halos $\times$ 150 lines of sight = 7500 points.

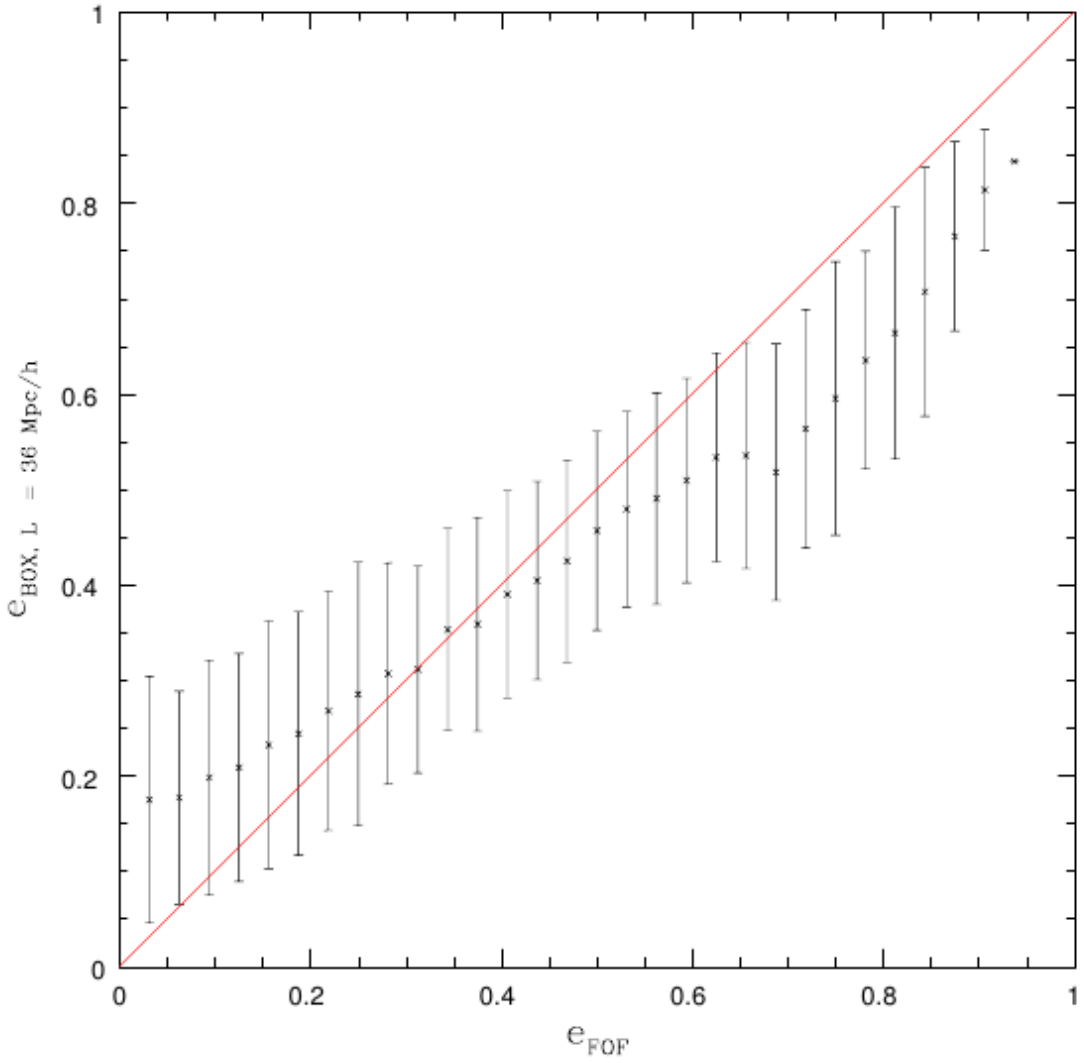

Figure 3.9: This plot shows the scatter in the ellipticity measurement when mass in a box around the halo is included. The box size for plot is $L = 36$ Mpc/h. Note that the window size is now 5 Mpc/h $\times$ 5 Mpc/h. Here e_{FOF} is the ellipticity measurement on just the FOF halo and e_{BOX} is the ellipticity measurement made after including mass along the line of sight. Note that in addition to the bias mentioned above, halos appear to be more spherical overall, but the effect is less when compared to Fig. 3.3. The error bars show the 1σ deviations and the plot was made with 50 halos $\times$ 150 lines of sight = 7500 points.

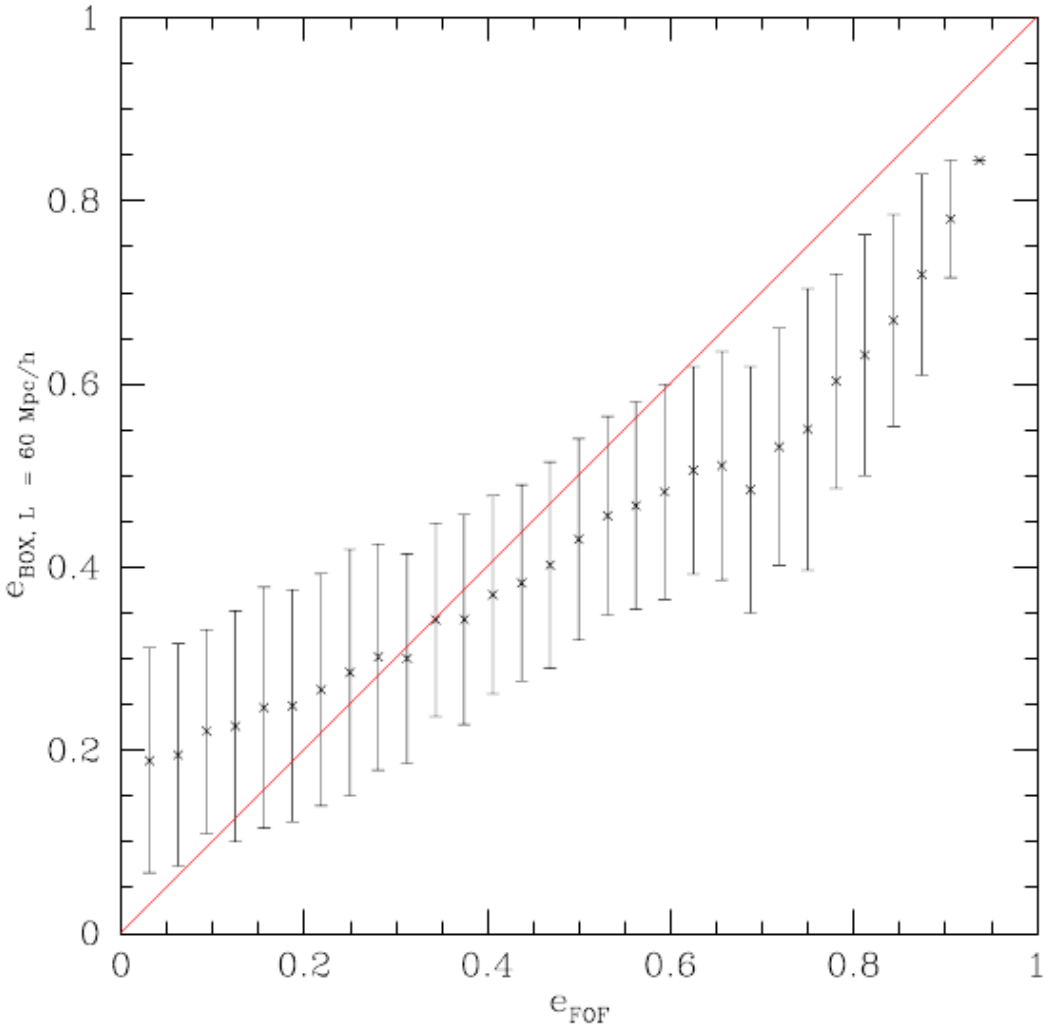

Figure 3.10: This plot shows the scatter in the ellipticity measurement when mass in a box around the halo is included. The box size for plot is $L = 60$ Mpc/h. Here e_{FOF} is the ellipticity measurement on just the FOF halo and e_{BOX} is the ellipticity measurement made after including mass along the line of sight. Note that in addition to the bias mentioned above, halos appear to be more spherical overall even more so then in Fig. 3.9, but less than Fig. 3.4. The error bars show the 1σ deviations and the plot was made with 50 halos $\times$ 150 lines of sight = 7500 points.

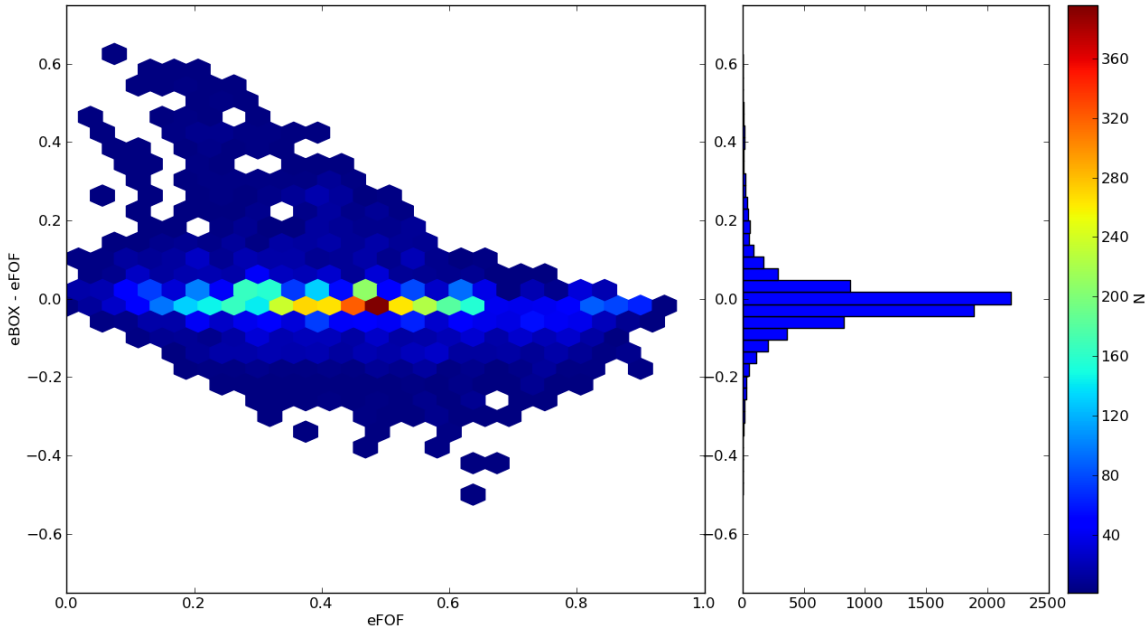

Figure 3.11: This plot is made from the same data as in Fig. 3.8, but here we show the scatter in the difference $e_{BOX} - e_{FOF}$. The plot in the right panel is a histogram of the $e_{BOX} - e_{FOF}$ values.

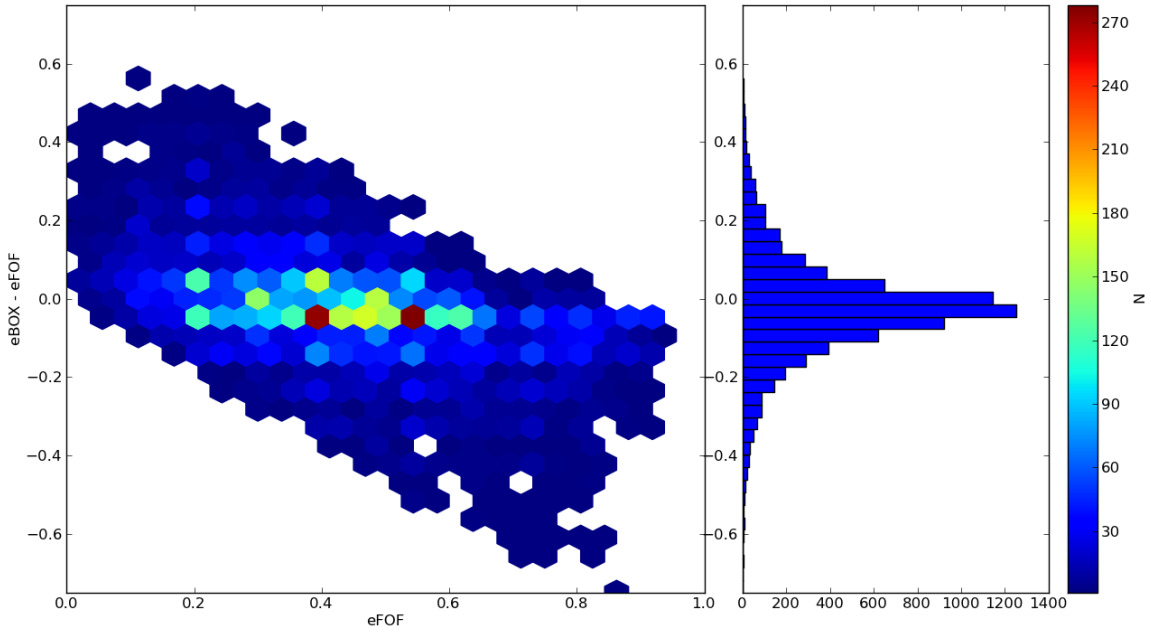

Figure 3.12: This plot is made from the same data as in Fig. 3.9, but here we show the scatter in the difference $e_{BOX} - e_{FOF}$. The plot in the right panel is a histogram of the $e_{BOX} - e_{FOF}$ values.

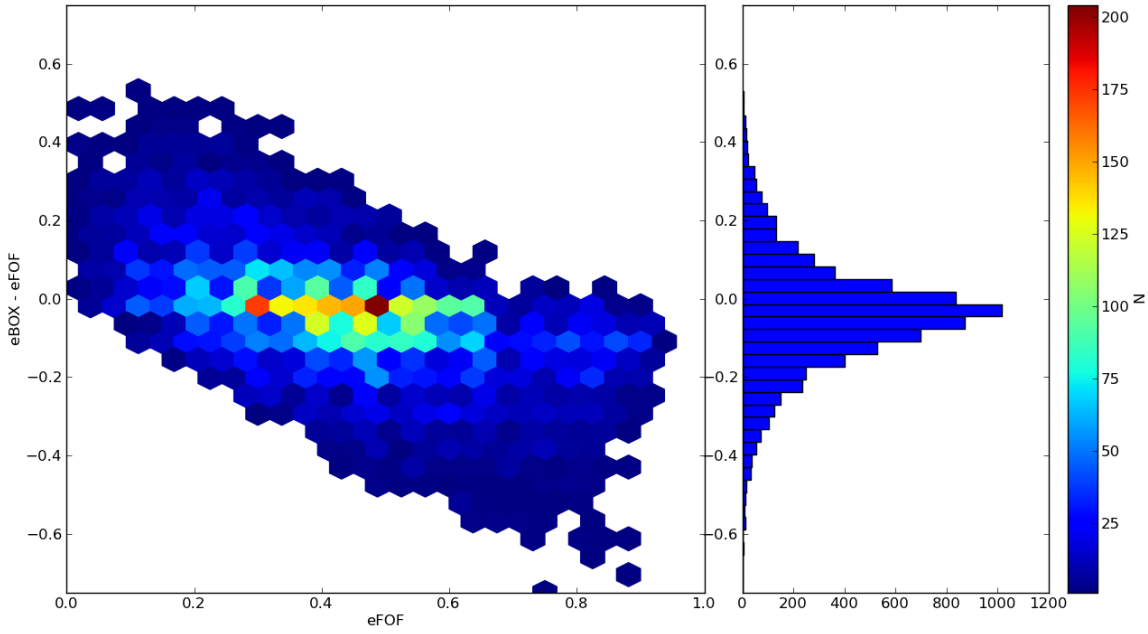

Figure 3.13: This plot is made from the same data as in Fig. 3.10, but here we show the scatter in the difference $e_{BOX} - e_{FOF}$. The plot in the right panel is a histogram of the $e_{BOX} - e_{FOF}$ values. Note how the peak is < 0 showing that halos appear more spherical.

And finally we do the exact same procedure for box dimensions, 3 Mpc × 3 Mpc × 2L

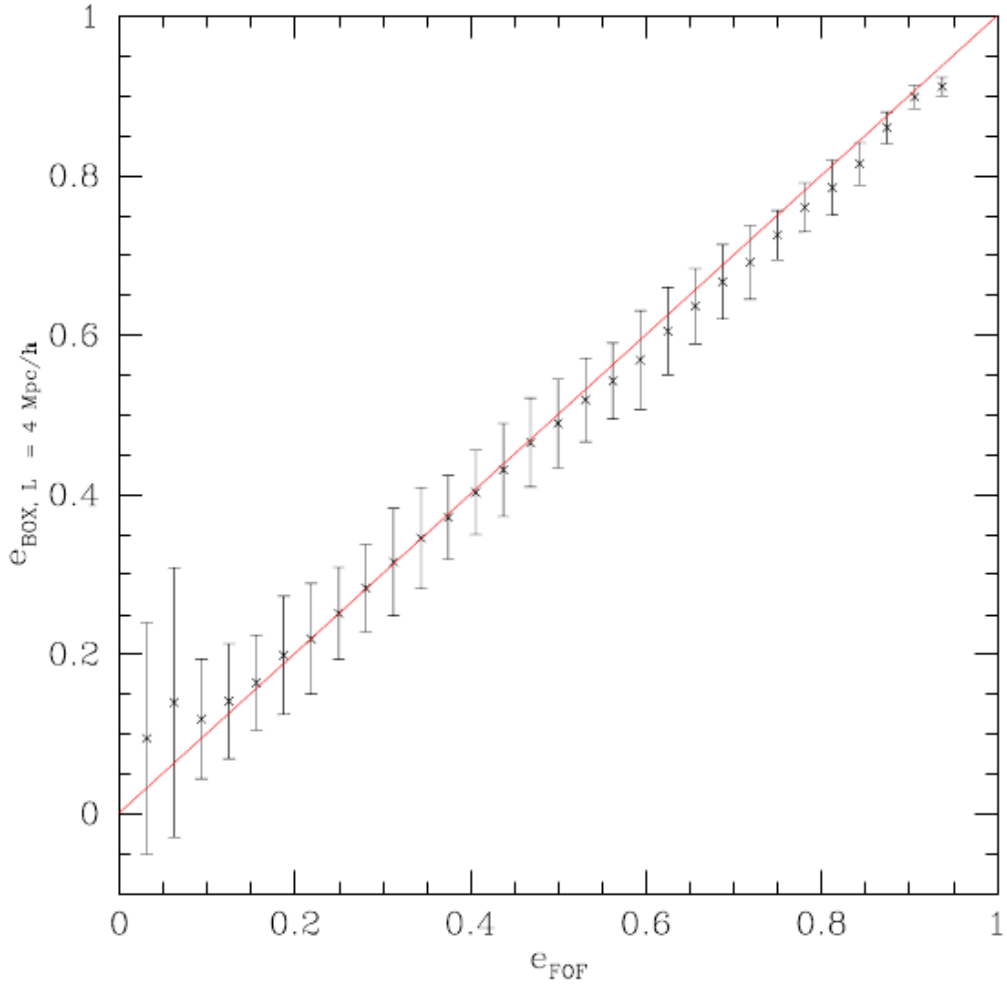

Figure 3.14: This plot shows the scatter in the ellipticity measurement when mass in a box around the halo is included. The box size for plot is $L = 4$ Mpc/h. Note that the window size is now 3 Mpc/h × 3 Mpc/h. Here e_{FOF} is the ellipticity measurement on just the FOF halo and e_{BOX} is the ellipticity measurement made after including mass along the line of sight. The bias that we saw in Fig. 3.2 and Fig. 3.8 is fairly suppressed. The error bars show the 1σ deviations and the plot was made with 50 halos × 150 lines of sight = 7500 points.

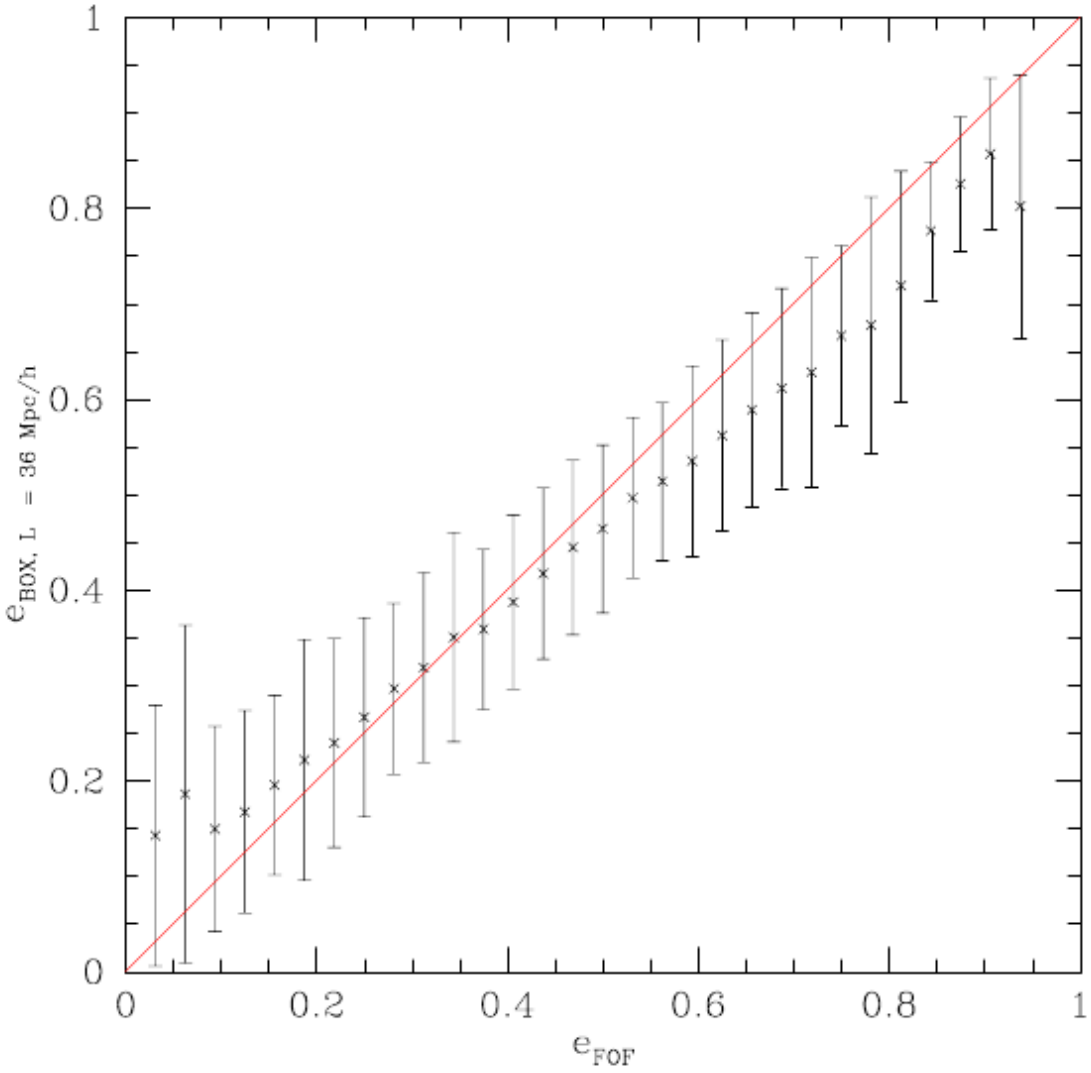

Figure 3.15: This plot shows the scatter in the ellipticity measurement when mass in a box around the halo is included. The box size for plot is $L = 36$ Mpc/h. Note that the window size is now 3 Mpc/h $\times$ 3 Mpc/h. Here e_{FOF} is the ellipticity measurement on just the FOF halo and e_{BOX} is the ellipticity measurement made after including mass along the line of sight. Here we see the halos do start to look spherical but the effect is less as compared to Fig. 3.3 and Fig. 3.9. The error bars show the 1σ deviations and the plot was made with 50 halos $\times$ 150 lines of sight = 7500 points.

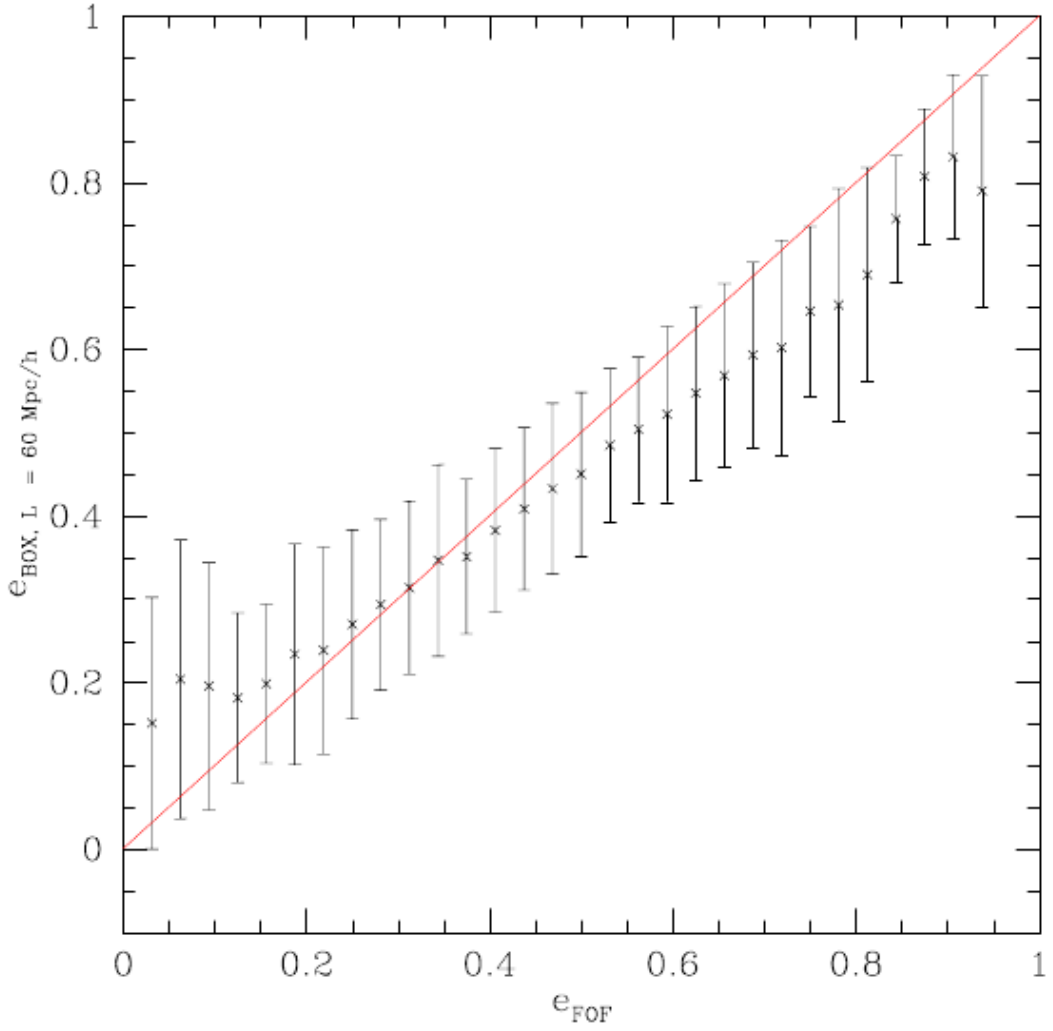

Figure 3.16: This plot shows the scatter in the ellipticity measurement when mass in a box around the halo is included. The box size for plot is $L = 60$ Mpc/h. Here e_{FOF} is the ellipticity measurement on just the FOF halo and e_{BOX} is the ellipticity measurement made after including mass along the line of sight. Note here that the spherical bias is enhanced as compared to Fig. 3.15 but is less when compared with Fig. 3.4 and Fig. 3.10. The error bars show the 1σ deviations and the plot was made with 50 halos $\times$ 150 lines of sight = 7500 points.

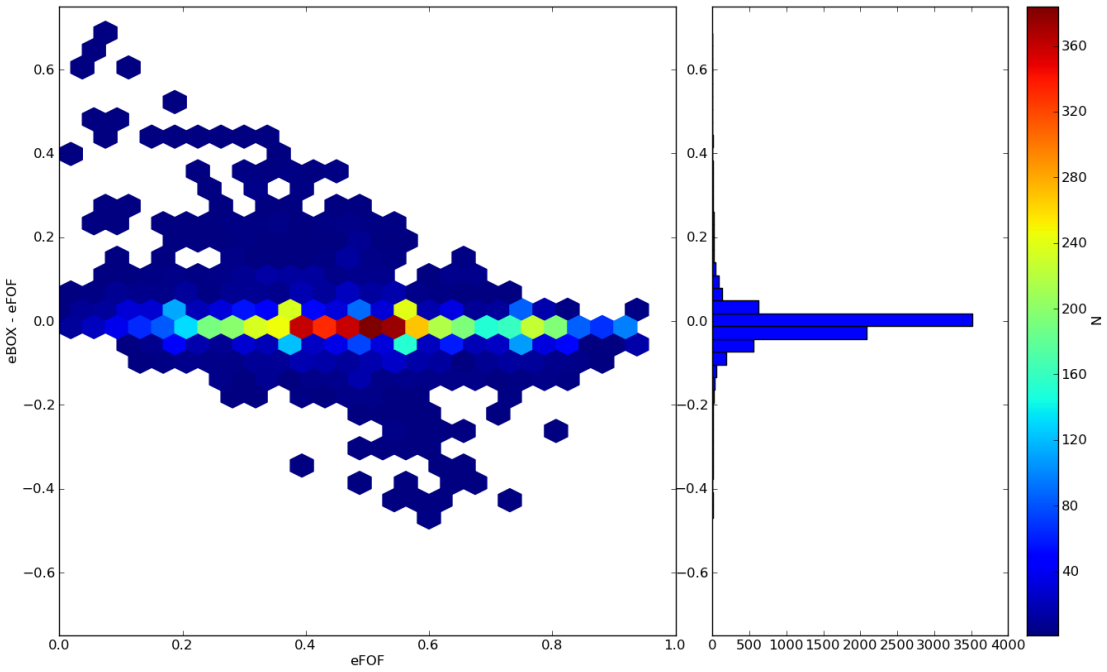

Figure 3.17: This plot is made from the same data as in Fig. 3.14, but here we show the scatter in the difference $e_{BOX} - e_{FOF}$. The plot in the right panel is a histogram of the $e_{BOX} - e_{FOF}$ values.

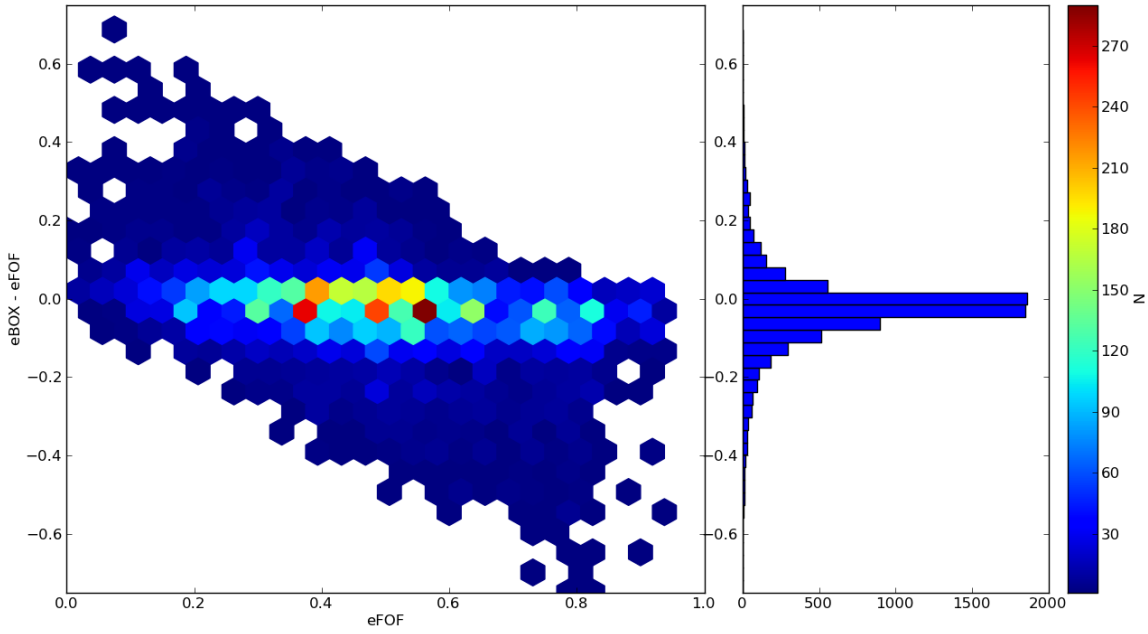

Figure 3.18: This plot is made from the same data as in Fig. 3.15, but here we show the scatter in the difference $e_{BOX} - e_{FOF}$. The plot in the right panel is a histogram of the $e_{BOX} - e_{FOF}$ values.

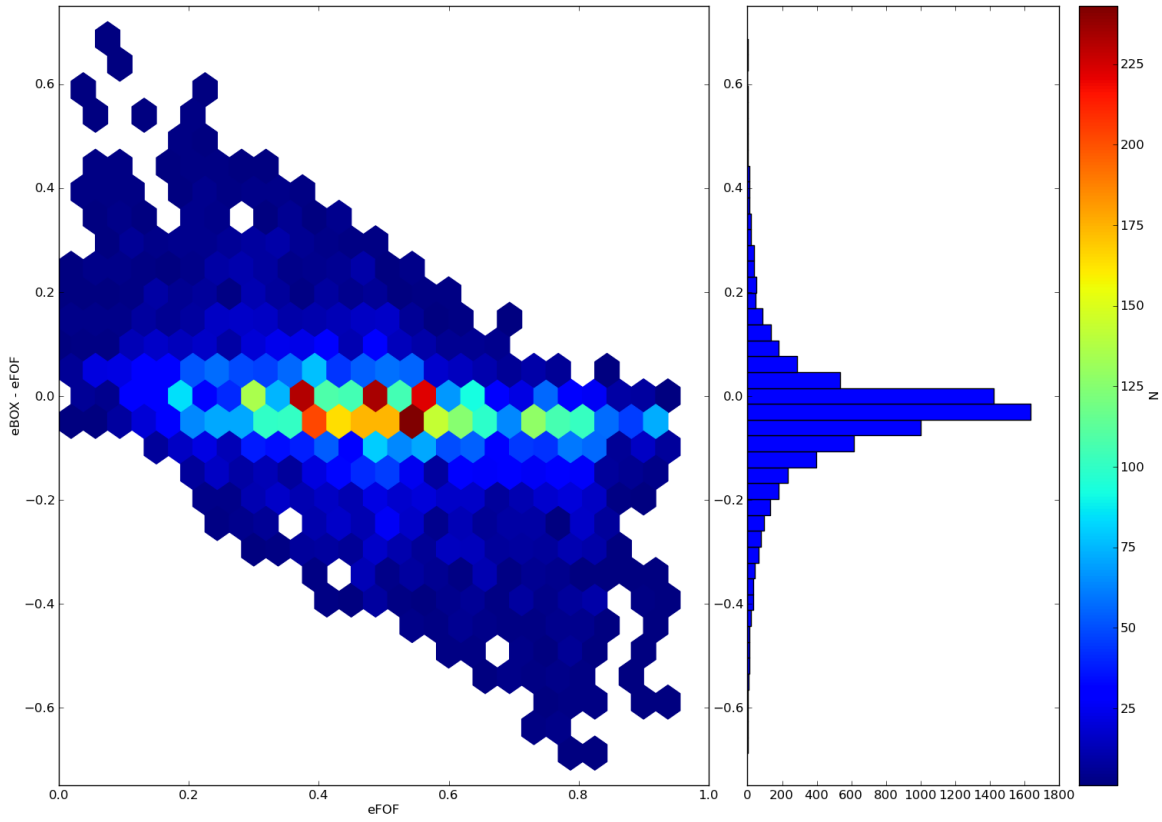

Figure 3.19: This plot is made from the same data as in Fig. 3.16, but here we show the scatter in the difference $e_{BOX} - e_{FOF}$. The plot in the right panel is a histogram of the $e_{BOX} - e_{FOF}$ values. Note how the peak is < 0 showing that halos appear more spherical.

3.3.2 Comparison of 3d and 2d Concentration

How concentrated a halo is depends on the parameter $c = R_{vir}/r_s$. Since there are two kinds of fits we can do, i.e., 2d and 3d, we get two concentrations. Recall that in Section 2.1 we used the particle with the highest local density as the centre of the halo for 3D NFW fits. To be consistent the same is done for the 2D fits rather than using the centre of mass. Note also that the best results for the 2d concentration were achieved when the window size for the 2d fitting grid was choosen to be 3 Mpc/h $\times$ 3 Mpc/h and a cut of $\bar{\chi}^2 \leq 50$ was applied to eliminate a few outliers[1]. where $\bar{\chi}^2$ is the reduced χ^2 value. This reduces the sample from 15000 to 11535 values, where the initial 15000 is obtained from the 100 most massive halos with 150 lines of sight each. Below are results for the comparison of these two concentrations, all data in this section is taken from Simulation 2.

The top panel of Fig. 3.20 shows a cumulative histogram for the range of c_{3d}/c_{2d} values for higher values of the elongation (less elliptical). No halos had $E \geq 0.8$. The bottom panel of Fig. 3.20 shows the same plot, but normalized. The color scheme is as follows;

Black	$0.0 \leq E < 0.2$
Green	$0.2 \leq E < 0.4$
Blue	$0.4 \leq E < 0.6$
Red	$0.6 \leq E < 0.8$

[1]The expected value for $\bar{\chi}^2$ is unity. But since the error/pixel we have chosen is just the Poisson error, $\sqrt{N}$, the error is underestimated. A fuller treatment of the statistics would be required for an ideal measurement, for e.g. see [48]. But for the purposes of theoretical trends of shape and concentration measurements with cosmological parameters like Ω_M and σ_8 we will see, in Section 3.3.3, that using just the Poisson error is found to be sufficient

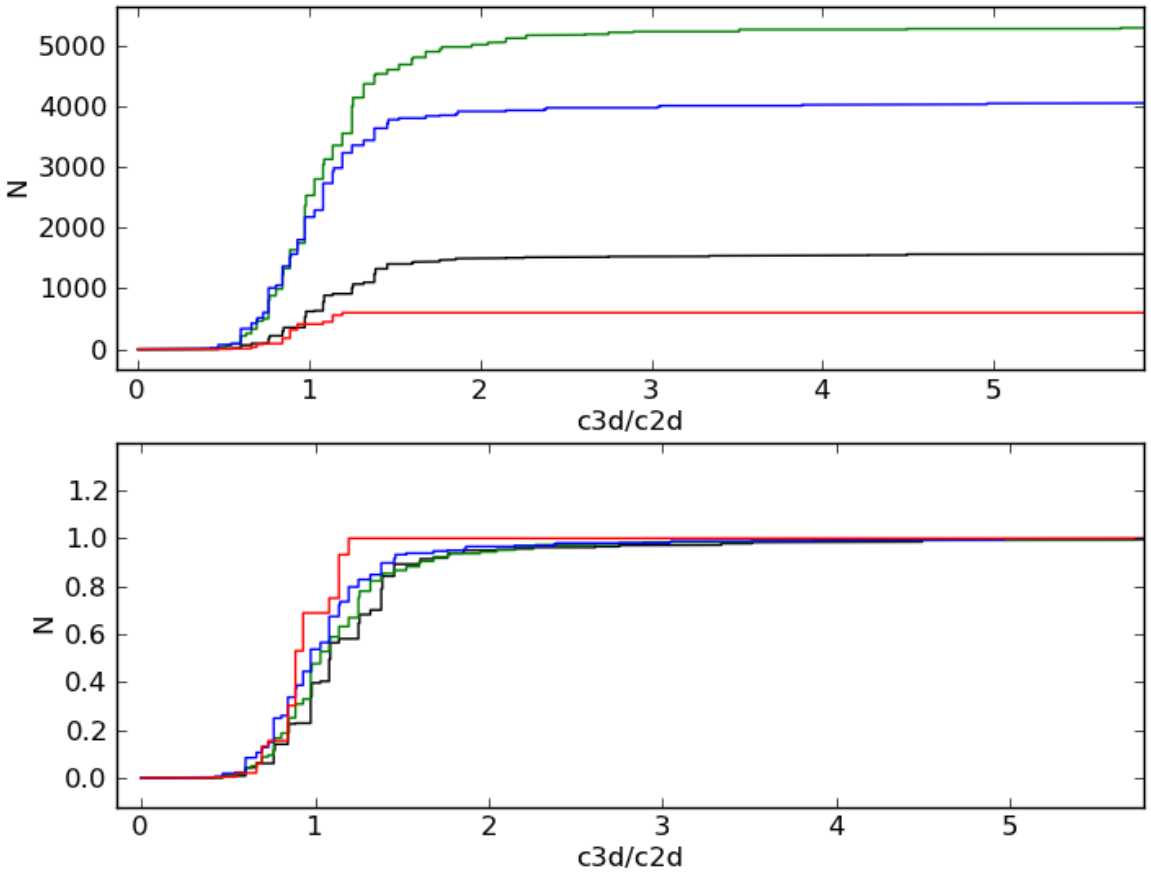

Figure 3.20: The top panel shows the cumulative histogram for all c_{3d}/c_{2d} values with the different colors showing different elongations. The bottom panel is the same as above but the data is normalized.

3.3.3 Tests with Modified Ω_M and σ_8

The final step of this project was to explore the effectiveness of shape measurements to break the degeneracy in Ω_M and σ_8. The procedure of this step is simple. As expressed in Section 3.1.4, three simulations were ran, Simulation 2 has the WMAP7 parameters and Simulation 1 and 3 have slightly different Ω_M and σ_8 (Simulation 1: $\Omega_M = 0.2$, $\sigma_8 = 0.9$ and Simulation 3: $\Omega_M = 0.35$, $\sigma_8 = 0.72$). 2d ellipticity measurements were made on all three simulations from top 100 halos with 150 lines of sight each. Note that these measurements are of e_{FOF}, i.e, without the contribution of LSS. Fig. 3.21 is a histogram of the e_{FOF} values and Fig. 3.22 is a normalized cumulative histogram for comparison. The color scheme is as follows,

Green	Simulation 1
Blue	Simulation 2
Red	Simulation 3

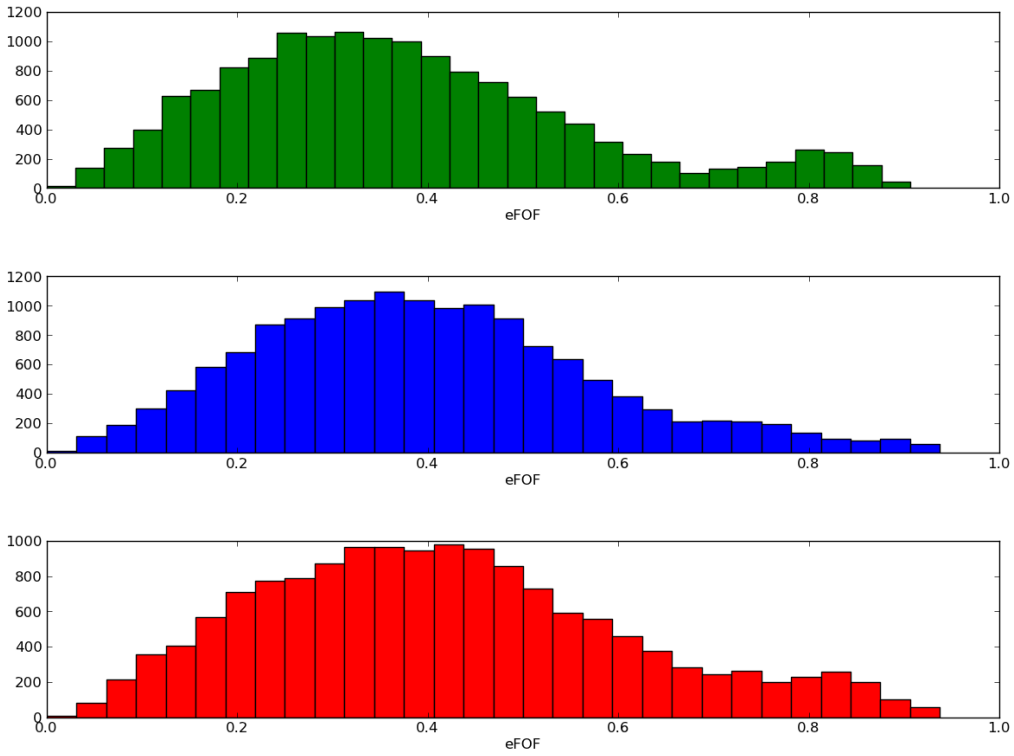

Figure 3.21: Histograms for e_{FOF} for the three simulations as described in Table 3.1. Note how the means are slightly shifted for each simulation.

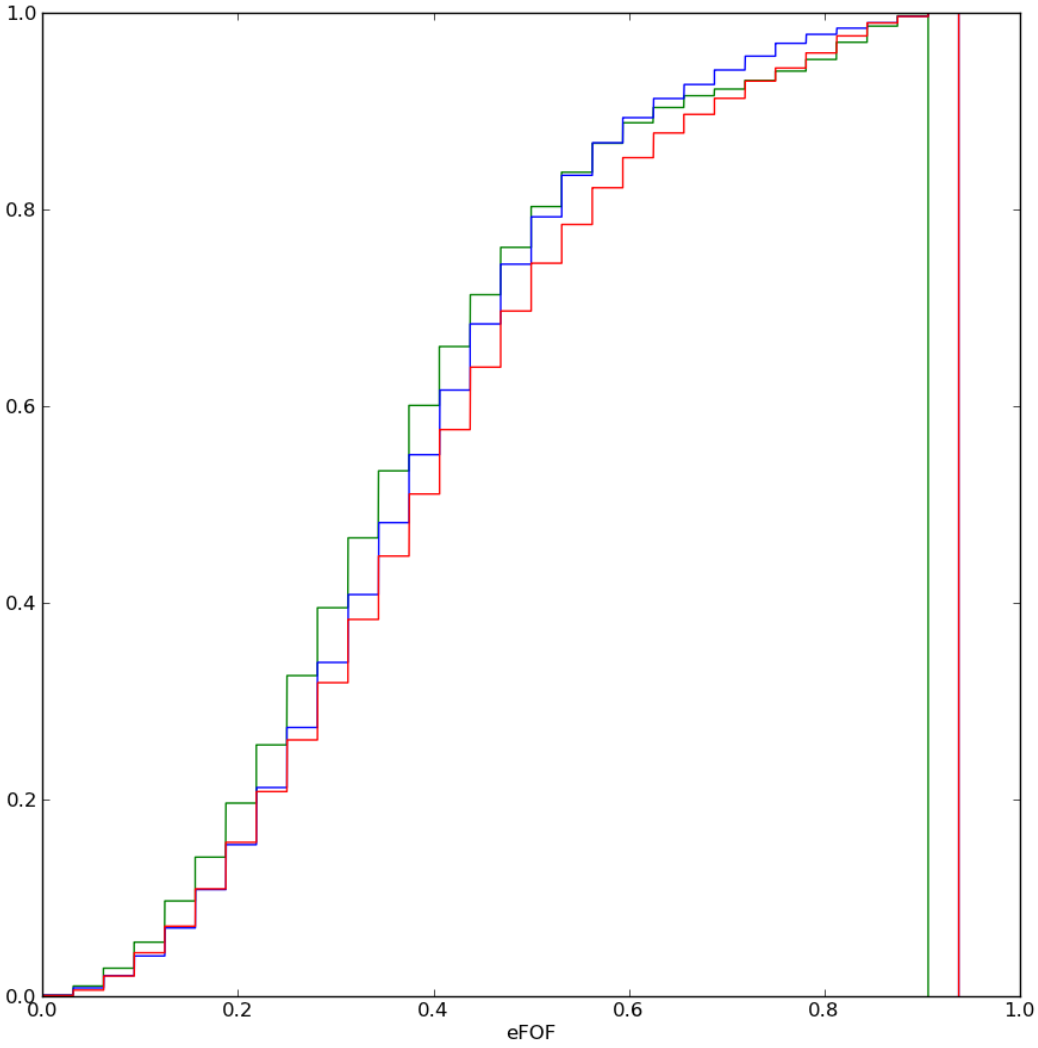

Figure 3.22: Cumulative normalized histogram for the three simulations as described in Table 3.1

We did the same for the 2d concentration measurements. Starting from an initial data set of 15000 for each simulation and then doing the $\bar{\chi}^2 \leq 50$ cut the sample sizes were reduced to the numbers shown in the following table. Fig. 3.23 and Fig. 3.24 are the analogs of Fig. 3.21 and Fig. 3.22, respectively and the color scheme is kept the same.

Simulation 1	12297
Simulation 2	11535
Simulation 3	12156

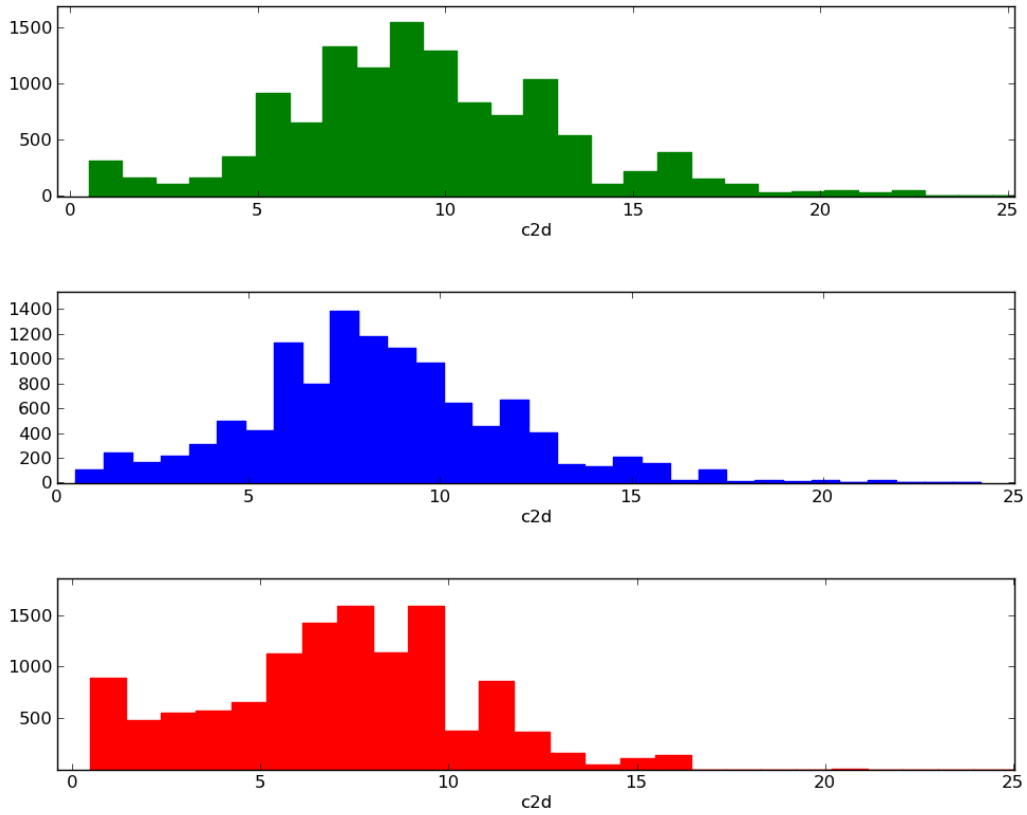

Figure 3.23: Histograms for c_{2d} for the three simulations as described in Table 3.1. Note how the means are slightly shifted for each simulation.

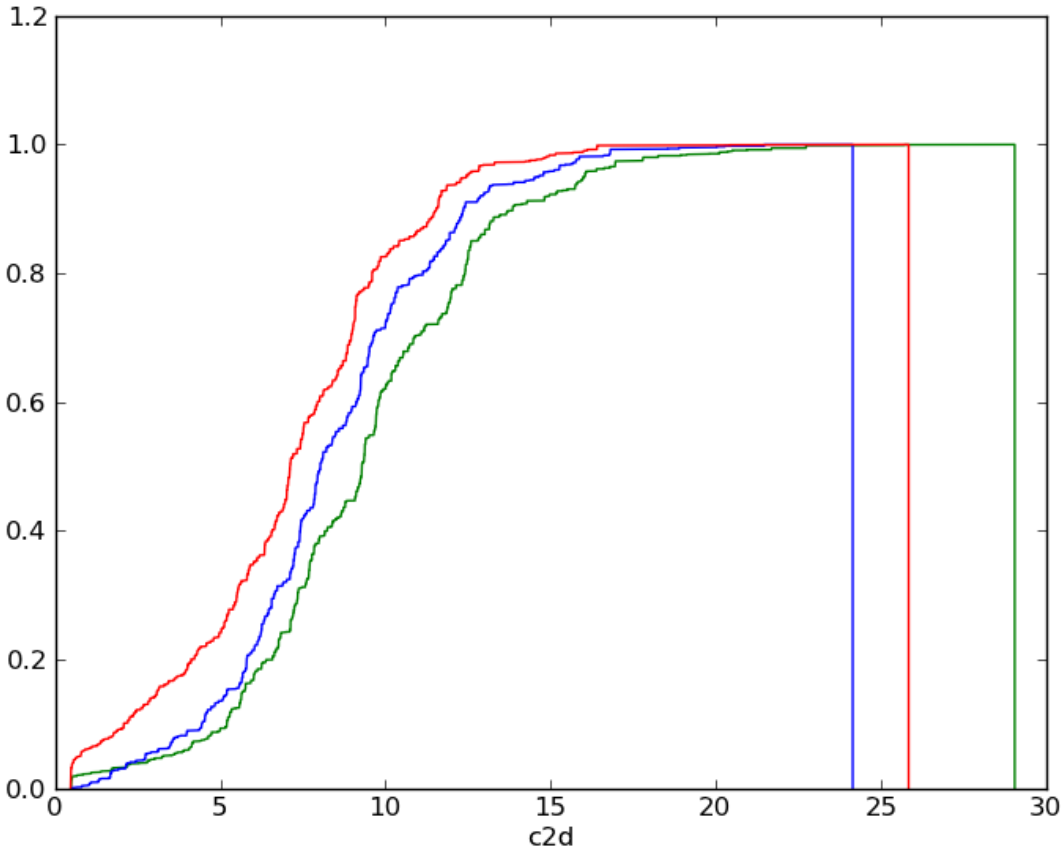

Figure 3.24: Cumulative normalized histogram c_{2d} for for the three simulations as described in Table 3.1

3.3.4 Lines of Sight Vs. Number of halos

The size of the data samples that we have used in the results shown above depends on the product of the number of lines of sight per halo and the number of halos. To measure the effect of mass along the line of sight and substructure in Section 3.3.1 we used 50 halos with 150 lines of sight each. This is a reasonable number to choose since we are interested

mainly in what the projection effects are, which are different for each line of sight. But after 150 random lines of sight, choosing more does not give enough new information about projection effects and that is why more halos are used, for e.g. to get a different distribution of substructure around the halo. In Section 3.3.2 a sample 100 halos and 150 lines of sight is chosen, this is because there is a cut on that data and that is why a bigger sample was created. For the last part, Section 3.3.3, increasing the halo sample is necessary to capture the physical trends caused by the changes in cosmological parameters. Taking many lines of sight on just a few halos will not show proper trends as those discussed in Chapter 2 since they are created from large halo samples.

Chapter 4

Discussion & Conclusion

4.1 Discussion

4.1.1 Effect of Large Scale Structure Along the Line of Sight

In Fig. 3.2 we see that there is a slight bias, halos which have a small e_{FOF} tend to have a higher e_{BOX} and halos which have a larger e_{FOF} tend to have a smaller e_{BOX}. Recall that Fig. 3.2 was for a box around the halo with dimensions 8 Mpc/h $\times$ 8 Mpc/h $\times$ 8 Mpc/h which means that it catches most of the substructure around the FOF halo without the diluting effects of noise that comes along the line of sight. The physical explanation for this bias is the following: for halos which are spherical, i.e. have a small e_{FOF}, any additional substructure that falls close to it will make the halo appear elliptical, atleast in the context of a χ^2-fit . As for the converse, halos which are highly elliptical, i.e. have a large e_{FOF}, any additional substructure that falls close to it will make the halo appear spherical. But when we decrease the field of view to 5 Mpc/h $\times$ 5 Mpc/h we see that this bias starts to get suppressed. For the case where the window size is chosen to be 3 Mpc/h $\times$ 3 Mpc/h, the bias is even further suppressed. This can be seen with low σ for the $L = 4$ Mpc/h case in Table 4.3 When longer box sizes are taken the bias on the

low end of ellipticities is enhanced, i.e for spherical values, and for all other values the ellipticity is reduced and halos appear to be more spherical. Figs. 3.5, 3.6, 3.7, 3.11, 3.12, 3.13, 3.17, 3.18 and 3.19 show scatter plots and an accompanying histogram that shows the distribution of $e_{BOX} - e_{FOF}$ vs e_{FOF}, the following tables show the mean and standard deviation of each plot.

L (Mpc/h)	μ	σ
4	-0.00437	0.104
36	-0.0341	0.156
60	-0.0617	0.168

Table 4.1: Mean, μ, and standard deviation, σ, for plots Figs. 3.5, 3.6 and 3.7.

L (Mpc/h)	μ	σ
4	-0.00850	0.0865
36	-0.0293	0.132
60	-0.0462	0.141

Table 4.2: Mean, μ, and standard deviation, σ, for plots Figs. 3.11, 3.12 and 3.13.

L (Mpc/h)	μ	σ
4	-0.00935	0.0574
36	-0.0303	0.107
60	-0.0406	0.118

Table 4.3: Mean, μ, and standard deviation, σ, for plots Figs. 3.17, 3.18 and 3.19.

We see that in the case of $L = 4$ Mpc/h the mean is $\mu \approx 0$ for all window sizes, which means that the above mentioned bias is almost canceled out when considering all values of e_{FOF}. As we increase L we see that the mean shifts more to the negative side and the

spread of the values increases. For $L = 60$ Mpc/h we see that the mean is, $\mu \approx -0.05$, which means that $e_{BOX} < e_{FOF}$ on average, this is due to diluting effect of the mass along the line of sight which makes halos appear to be more spherical.

4.1.2 Comparison of 3d and 2d Concentration

For the investigation of the relationship between the 3d and 2d concentration Fig. 3.20 was provided. The results are fairly intuitive to understand. From Table 4.4 we see that the elongation ranges $0 \leq E < 0.2$ and $0.2 \leq E < 0.4$ have the highest standard deviation, σ. Recall that these two ranges consist of halos that are highly elliptical and the 3D profile that is fitted is not triaxial. This is the most likely cause of the high standard deviation. Especially when we see that for the halos that are fairly spherical,$0.4 \leq E < 0.6$ and $0.6 \leq E < 0.8$, the scatter is much less. Aside from the triaxiality the substructure close to the halo that gets included in the FOF process also contributes to the scatter.

E	μ	σ
$0.0 \leq E < 0.2$ (Black)	1.26	0.938
$0.2 \leq E < 0.4$ (Green)	1.20	0.989
$0.4 \leq E < 0.6$ (Blue)	1.08	0.538
$0.6 \leq E < 0.8$ (Red)	0.935	0.163

Table 4.4: Mean, μ, and standard deviation, σ, for plot in Fig. 3.20

4.1.3 Tests with Modified Ω_M and σ_8

In Section 1.3.2 we discussed that there is a degeneracy between Ω_m and σ_8 and how it can potentially be broken by making shape measurements. We make efforts in trying to break this degeneracy. We saw why a high value of σ_8 resulted in halos that are more spherical than those produced by a low value of σ_8. Our aim is too see if we can pick up this effect

by measuring the 2d ellipticities of halos in different cosmologies. We use halos from three different simulations with different values of $\sigma_8$and Ω_M and make measurements of e_{FOF}, i.e. without any noise. In Fig. 3.22 we see the result of these measurements. Recall that Fig. 3.22 was made from 100 halos $\times$ 150 lines of sight which gives 15000 points from each simulation. We note that there is indeed some distinction in the shape measurements across the three simulations. As expected in Simulation 1 (Green) we see halos tend to be slightly more spherical and in Simulation 3 (Red) we see halos that are slightly more elliptical then the WMAP7 Simulation 2 (Blue). But how different are these simulations? We can test this by sampling values from each simulation and performing a KS-Test. The sample sizes we choose are $N = 10$, 100, 1000, 5000 and 10000. We extract samples for each N 100 times and compute the average for the p-value and for D, where D is the maximum distance between the two normalized cumulative distribution curves. The results for this are summarized in the following two tables. Table 4.5 shows the results for the comparison between Simulation 1 and Simulation 2 and Table 4.6 shows the result between Simulation 2 and Simulation 3. Note that the null hypotheses here is that the two distributions are the same when doing the KS-test and in both cases it is only rejected at approximately the 4 σ level when N =5000 and exceeds the 5 σ level for N = 10000.

N	D	p-value	σ-level
10	0.305	0.656	0.575σ
100	0.128	0.466	0.729σ
1000	0.0689	0.0877	1.71σ
5000	0.0594	1.34×10^{-5}	4.35σ
10000	0.0586	4.73×10^{-9}	5.85σ

Table 4.5: KS-Test results for e_{FOF} comparison between Simulation 1 and Simulation 2

N	D	p-value	σ-level
10	0.342	0.560	0.582σ
100	0.113	0.564	0.577σ
1000	0.0602	0.146	1.45σ
5000	0.0519	1.83×10^{-4}	3.74σ
10000	0.0521	9.74×10^{-9}	5.73σ

Table 4.6: KS-Test results for e_{FOF} comparison between Simulation 3 and Simulation 2

We do above analysis for the concentration values across all three simulations as well. The results were shown in Fig. 3.23 and Fig. 3.24. As per the discussions in Section 2.2, specifically, the trends pointed out in Section 2.2.5, it is expected that Simulation 1 would have halos which are more concentrated because they are older and Simulation 3 would have halos which are less concentrated because they are younger. The trends that we see in Fig. 3.23 and Fig. 3.24 are consistent with these expectations. We do a similar KS-test as above for the concentrations, the results are summarized in Table 4.7 and 4.8. We see that the null hypothesis is rejected at the 3 σ level for N=500 and exceeds 5 σ level for N=1000.

N	D	p-value	σ-level
10	0.356	0.526	0.634σ
100	0.198	0.130	1.51σ
500	0.162	8.28×10^{-4}	3.34σ
1000	0.165	3.34×10^{-8}	5.52σ

Table 4.7: KS-Test results for c_{2d} comparison between Simulation 1 and Simulation 2

N	D	p-value	σ-level
10	0.394	0.430	0.789σ
100	0.216	0.0639	1.85σ
500	0.187	2.18×10^{-5}	4.24σ
1000	0.180	1.03×10^{-10}	6.11σ

Table 4.8: KS-Test results for c_{2d} comparison between Simulation 3 and Simulation 2

4.2 Conclusion & Outlook

In Chapter 1 we saw in some detail how the universe started in a big bang and expanded to what we see today. During this expansion we learned how dark matter played a crucial role in the formation of the structure we see today and how all of this is quantified in the ΛCDM model. Towards the end of Chapter 1 we saw how observational data from clusters can help constrain Ω_M and σ_8. Chapter 2 provided insight into the importance of the shapes of a halo as a good tracer of halo properties. We saw that it was closely related to the age and concentration of the halo. How weak lensing could be used to measure said shape was also discussed. In Chapter 3 the inner workings of GADGET were briefly discussed together with the details of the three simulations that were run for this project. Next the methodology used was discussed and the results were presented. In this last section we provide some concluding remarks for the results obtained.

On the bias introduced by substructure: We saw that the substructure immediately close to the halo was a significant factor which contaminated the measurement of the ellipticity. The bias found was that spherical halos were measured as slightly elliptical and elliptical halos were measured as slightly spherical. However this was fairly suppressed by using a smaller window size. Using a smaller window size, however, could also mean that the method is more sensitive to the inner core of the halo. Note that one shortcoming of the method was to fix the center of the halo at the center of mass. This was done mainly

to save computational time and picking the BCG was out of the question because baryons were not included in the analysis. Note also that another effect was of halos appearing more spherical with a longer line of sight. This was, of course, due to the mass along the line of sight. This is problem is common when making just mass measurements of halos through lensing, one resolution to this is to subtract off the predicted cosmic shear which can be computed from the power spectrum, see for e.g. [39] [27] [18].

On the measurement of concentration: Here the findings are consistent with expectations. Given that the c_{3d} was fit with a spherical profile and c_2d took account for the ellipticity of the halos; the highest scatters were seen in the halos that were the most elliptical. For halos the were close to being spherical the scatter was minimised.

On shape measurements with modified Ω_M and σ_8: The final part of the project was to check if shape measurements can be used to alleviate the degeneracy in Ω_M and σ_8 as discussed in Section 1.3. For this purpose three simulations were run. Simulation 2 had WMAP7 parameters, Simulation 1 had a slightly lower value for Ω_M and a slightly higher value for σ_8, and the converse was true in Simulation 3. In Fig 3.22 we saw that there was a slight difference in the ellipticity measured, Simulation 1 halos were slightly less elliptical, Simulation 2 halos were more elliptical and Simulation 3 halos were the most elliptical. Note that this was done for a sample of 100 halos $\times$ 150 lines of sight = 15000 data points. Then in Tables 4.5 and 4.6 we performed a KS-test to see how many measurements of the ellipticity would be required to spot the difference between the distribution of ellipticity of each halo. The result was that at least 3000 halos were required to spot a difference from Simulation 2 at a confidence level of 3σ. Currently high resolution weak lensing studies for shapes provide sample sizes of $\sim$ 20 to 25 halos [48] [47] [17] [59]. With ongoing surveys like SPT, ACT and Planck this number is increasing and is expected to go up to $\sim$ 1000 [2]. A mammoth sized catalog of clusters is expected from eROSITA, it is estimated to detect about 50000 to 100000 clusters through X-ray emission [21]. Further projects aimed specifically at weak lensing include the LSST, KiDs, WIRE. Even further, upcoming projects like EUCLID [22] should provide larger samples with very high accuracy. But note that there is a shortcoming, however, the ellipticities

that are measured do not include the effect of mass along the line of sight and are measured from just the FOF halo in projection. Therefore, I claim that this is purely a theoretical effect that can be picked up in numerical simulations. If such measurements turn out to be feasible, then figuring out the best way to anaylze them will require further work. When the same analysis is done, however, for the concentrations (Fig. 3.24) we see that concentration measurements are a better probe than shape measurements.

Appendix A

Moment of Inertia Tensor

We note that the diagonal form of the moment of inertia tensor of a solid, uniform density, ellipsoid of mass M is given by;

$$\lambda^E = K \begin{bmatrix} (b^2+c^2) & 0 & 0 \\ 0 & (a^2+c^2) & 0 \\ 0 & 0 & (a^2+b^2) \end{bmatrix} \tag{A.1}$$

where $K = M/5$ and, a, b and c are the axes of the ellipsoid. The moment of inertia I for an arbitrary mass distribution is given by,

$$I_{ij} = \sum_k m_k (r_k^2 \delta_{ij} - r_{k,i} r_{k,j}) \tag{A.2}$$

Say, λ is the diagonal matrix for I. Then to fit an ellipsoid over the mass distribution we simply ask what values of a, b and c solve the equation $\lambda^E = \lambda$. This gives us the following three equations.

$$a^2 = \frac{1}{2K}(-\lambda_1 + \lambda_2 + \lambda_3) \tag{A.3}$$

$$b^2 = \frac{1}{2K}(\lambda_1 - \lambda_2 + \lambda_3) \tag{A.4}$$

$$c^2 = \frac{1}{2K}(\lambda_1 + \lambda_2 - \lambda_3) \tag{A.5}$$

where the λ_i are the diagonal entries of λ. Now we assume that there is some matrix $\tilde{I}$ such that its diagonal matrix $\tilde{\lambda}$ has entries a^2, b^2 and c^2. We also assume that P, the eigenvector matrix, is the same for I and $\tilde{I}$. Now we can write the following;

$$\tilde{\lambda} = \frac{1}{2K}\left[\mathrm{tr}(\lambda)I_3 - 2\lambda\right] \tag{A.6}$$

where I_3 is the 3-dimensional identity matrix. Left multiplying the above with P and right multiplying by P^{-1} gives us;

$$\tilde{I} = \frac{1}{2K}\left[\mathrm{tr}(I)I_3 - 2I\right] \tag{A.7}$$

where we have made use of the identity $\mathrm{tr}(I) = \mathrm{tr}(\lambda)$. When we plug in the full form of I from Eq. A.2 in the above equation we get the desired result;

$$\tilde{I}_{ij} = \frac{1}{K}\sum_k m_k r_{k,i} r_{k,j}. \tag{A.8}$$

References

[1] P.A.R. Ade et al. Planck Early Results VIII: The all-sky Early Sunyaev-Zeldovich cluster sample. *Astron.Astrophys.*, 536, 2011.

[2] Steven W. Allen, August E. Evrard, and Adam B. Mantz. Cosmological Parameters from Observations of Galaxy Clusters. *Ann.Rev.Astron.Astrophys.*, 49:409–470, 2011.

[3] Brandon Allgood, Ricardo A. Flores, Joel R. Primack, Andrey V. Kravtsov, Risa H. Wechsler, et al. The shape of dark matter halos: dependence on mass, redshift, radius, and formation. *Mon.Not.Roy.Astron.Soc.*, 367:1781–1796, 2006.

[4] Monqiue Arnaud, E. Pointecouteau, and G.W. Pratt. The Structural and scaling properties of nearby galaxy clusters. 2. The M-T relation. *Astron.Astrophys.*, 441:893–903, 2005.

[5] D. A. Ostlie B. W. Carroll. *An Introduction to Modern Astrophysics*. Addison-Wesley, 2007.

[6] Matthias Bartelmann. Arcs from a universal dark matter halo profile. *Astron.Astrophys.*, 313:697–702, 1996.

[7] Matthias Bartelmann and Peter Schneider. Weak gravitational lensing. *Phys.Rept.*, 340:291–472, 2001.

[8] P. Bett, V. Eke, C. S. Frenk, A. Jenkins, J. Helly, and J. Navarro. The spin and shape of dark matter haloes in the Millennium simulation of a Λ cold dark matter universe. *Mon.Not.Roy.Astron.Soc.*, 376:215–232, March 2007.

[9] Stefano Borgani. Cosmology with clusters of galaxies. *Lect.Notes Phys.*, 2006.

[10] Thomas J. Broadhurst et al. Strong lensing analysis of A1689 from deep Advanced Camera images. *Astrophys.J.*, 621:53–88, 2005.

[11] Thomas J. Broadhurst, Masahiro Takada, Keiichi Umetsu, Xu Kong, Nobuo Arimoto, et al. The Surprisingly steep mass profile of Abell 1689, from a lensing analysis of Subaru images. *Astrophys.J.*, 619:L143, 2005.

[12] S. E. Bryan, S. T. Kay, A. R. Duffy, J. Schaye, C. Dalla Vecchia, and C. M. Booth. The impact of baryons on the spins and shapes of dark matter haloes. *ArXiv e-prints*, July 2012.

[13] D. A. Buote and P. J. Humphrey. Spherically averaging ellipsoidal galaxy clusters in X-ray and Sunyaev-Zel'dovich studies - I. Analytical relations. *Mon.Not.Roy.Astron.Soc.*, 420:1693–1705, February 2012.

[14] J.E. Carlstrom, P.A.R. Ade, K.A. Aird, B.A. Benson, L.E. Bleem, et al. The 10 Meter South Pole Telescope. *Publ.Astron.Soc.Pac.*, 123:568–581, 2011.

[15] Douglas Clowe, Marusa Bradac, Anthony H. Gonzalez, Maxim Markevitch, Scott W. Randall, et al. A direct empirical proof of the existence of dark matter. *Astrophys.J.*, 648:L109–L113, 2006.

[16] Douglas Ian Clowe, G. De Lucia, and L. King. Effects of asphericity and substructure on the determination of cluster mass with weak gravitational lensing. *Mon.Not.Roy.Astron.Soc.*, 350:1038, 2004.

[17] V. L. Corless, L. J. King, and D. Clowe. A new look at massive clusters: weak lensing constraints on the triaxial dark matter haloes of A1689, A1835 and A2204. *Mon.Not.Roy.Astron.Soc.*, 393:1235–1254, March 2009.

[18] Scott Dodelson. Cluster masses accounting for structure along the line of sight. *Phys.Rev.*, D70:023008, 2004.

[19] J. Dubinski. The effect of dissipation on the shapes of dark halos. *Astrophys.J.*, 431:617–624, August 1994.

[20] DUNE Website. http://www.dune-mission.net/.

[21] eROSITA Website. http://www.mpe.mpg.de/eROSITA.

[22] EUCLID Website. http://sci.esa.int/euclid/.

[23] C. S. Frenk, S. D. M. White, M. Davis, and G. Efstathiou. The formation of dark halos in a universe dominated by cold dark matter. *Astrophys.J.*, 327:507–525, April 1988.

[24] Liang Gao, Volker Springel, and Simon D.M. White. The Age dependence of halo clustering. *Mon.Not.Roy.Astron.Soc.*, 363:L66–L70, 2005.

[25] Raphael Gavazzi. Projection effects in cluster mass estimates: The Case of MS2137-23. *Astron.Astrophys.*, 2005.

[26] E. Hayashi, J.F. Navarro, and V. Springel. The Shape of the Gravitational Potential in Cold Dark Matter Halos. *Mon.Not.Roy.Astron.Soc.*, 377:50–62, 2007.

[27] H. Hoekstra. The effect of distant large scale structure on weak lensing mass estimates. *Astronomy and Astrophysics*, 370:743–753, May 2001.

[28] E. Hubble. A Relation between Distance and Radial Velocity among Extra-Galactic Nebulae. *Proceedings of the National Academy of Science*, 15:168–173, March 1929.

[29] Akila Jeeson-Daniel, Claudio Dalla Vecchia, Marcel R. Haas, and Joop Schaye. The correlation structure of dark matter halo properties. 2011.

[30] Y.P. Jing and Yasushi Suto. Density profiles of dark matter halo are not universal. *Astrophys.J.*, 529:L69–72, 2000.

[31] Y.P. Jing and Yasushi Suto. Triaxial modeling of halo density profiles with high-resolution N-body simulations. *Astrophys.J.*, 574:538, 2002.

[32] Y.P. Jing, Yasushi Suto, and H.J. Mo. The dependence of dark halo clustering on the formation epoch and the concentration parameter. *Astrophys.J.*, 657:664–668, 2007.

[33] S.F. Kasun and August E. Evrard. Shapes and alignments of galaxy cluster halos. *Astrophys.J.*, 629:781–790, 2005.

[34] Stelios Kazantzidis, Andrey V. Kravtsov, Andrew R. Zentner, Brandon Allgood, Daisuke Nagai, et al. The Effect of gas cooling on the shapes of dark matter halos. *Astrophys.J.*, 611:L73–L76, 2004.

[35] Arthur Kosowsky. The Atacama Cosmology Telescope Project: A Progress Report. *New Astron.Rev.*, 50:969–976, 2006.

[36] A. V. Kravtsov, A. Klypin, and Y. Hoffman. Constrained Simulations of the Real Universe. II. Observational Signatures of Intergalactic Gas in the Local Supercluster Region. *Astrophys.J.*, 571:563–575, June 2002.

[37] T.A. Marriage, V. Acquaviva, P.A.R. Ade, P. Aguirre, M. Amiri, et al. The Atacama Cosmology Telescope: Sunyaev Zel'dovich Selected Galaxy Clusters at 148 GHz in the 2008 Survey. *Astrophys.J.*, 737:61, 2011.

[38] Massimo Meneghetti, Matthias Bartelmann, and Adrian Jenkins. The effects of ellipticity and substructure on estimates of cluster density profiles based on lensing and kinematics. *Mon.Not.Roy.Astron.Soc.*, 381:171–186, 2007.

[39] C. A. Metzler, M. White, and C. Loken. The Effect of the Cosmic Web on Cluster Weak Lensing Mass Estimates. *Astrophys.J.*, 547:560–573, February 2001.

[40] Christopher A. Metzler, Martin J. White, Michael Norman, and Chris Loken. Weak gravitational lensing and cluster mass estimates. *Astrophys.J.*, 520:L9, 1999.

[41] Millennium Website. www.mpa-garching.mpg.de/galform/millennium/.

[42] NASA Website. http://apod.nasa.gov/.

[43] Julio F. Navarro, Carlos S. Frenk, and Simon D.M. White. The Structure of cold dark matter halos. *Astrophys.J.*, 462:563–575, 1996.

[44] N-Body Shop, University of Washington. http://www-hpcc.astro.washington.edu/tools/tools.html.

[45] Nobel Prize Website. http://www.nobelprize.org.

[46] P.E.J. Nulsen, S.L. Powell, and A. Vikhlinin. Model-independent X-ray mass determinations. *Astrophys.J.*, 722:55–64, 2010.

[47] Masamune Oguri, Matthew B. Bayliss, Haakon Dahle, Keren Sharon, Michael D. Gladders, et al. Combined strong and weak lensing analysis of 28 clusters from the Sloan Giant Arcs Survey. *Mon.Not.Roy.Astron.Soc.*, 420:3213–3239, 2012.

[48] Masamune Oguri, Masahiro Takada, Nobuhiro Okabe, and Graham P. Smith. Direct measurement of dark matter halo ellipticity from two-dimensional lensing shear maps of 25 massive clusters. *Mon.Not.Roy.Astron.Soc.*, 405:2215–2230, 2010.

[49] T. Padmanabhan. *Structure Formation in the Universe*. Cambridge University Press, 1993.

[50] J. A. Peacock. *Cosmological Physics*. Cambridge University Press, 1998.

[51] S. Perlmutter et al. Measurements of Omega and Lambda from 42 high redshift supernovae. *Astrophys.J.*, 517:565–586, 1999.

[52] Planck Website. http://www.esa.int/SPECIALS/Planck/index.html.

[53] M. Postman, L.M. Lubin, J.E. Gunn, J.B. Oke, J.G. Hoessel, et al. The Palomar Distant Cluster Survey. 1. The Cluster Catalog. *Astron.J.*, 111:615, 1996.

[54] W. H. Press and P. Schechter. Formation of Galaxies and Clusters of Galaxies by Self-Similar Gravitational Condensation. *Astrophys.J.*, 187:425–438, February 1974.

[55] Adam G. Riess et al. Observational evidence from supernovae for an accelerating universe and a cosmological constant. *Astron.J.*, 116:1009–1038, 1998.

[56] ROSAT Website. http://heasarc.gsfc.nasa.gov/.

[57] B. S. Ryden. *Introduction to Cosmology*. Addison-Wesley, 2002.

[58] D. Chilko S. Dowdy, S. Wearden. *Statistics for Research*. Wiley, 2004.

[59] M. Sereno and A. Zitrin. Triaxial strong-lensing analysis of the z ¿ 0.5 MACS clusters: the mass-concentration relation. *Mon.Not.Roy.Astron.Soc.*, 419:3280–3291, February 2012.

[60] R. A. Skibba and A. V. Macciò. Properties of dark matter haloes and their correlations: the lesson from principal component analysis. *Mon.Not.Roy.Astron.Soc.*, 416:2388–2400, September 2011.

[61] SPITZER Website. http://www.spitzer.caltech.edu/.

[62] Volker Springel. The Cosmological simulation code GADGET-2. *Mon.Not.Roy.Astron.Soc.*, 364:1105–1134, 2005.

[63] K. Vanderlinde, T.M. Crawford, T. de Haan, J.P. Dudley, L. Shaw, et al. Galaxy Clusters Selected with the Sunyaev-Zel'dovich Effect from 2008 South Pole Telescope Observations. *Astrophys.J.*, 722:1180–1196, 2010.

[64] Alexey Vikhlinin, A. Kravtsov, W. Forman, C. Jones, M. Markevitch, et al. Chandra sample of nearby relaxed galaxy clusters: Mass, gas fraction, and mass-temperature relation. *Astrophys.J.*, 640:691–709, 2006.

[65] You-Gang Wang and Z.-H. Fan. Systematic errors in the determination of hubble constant due to the asphericity and non-isothermality of clusters of galaxies. *Astrophys.J.*, 643:630–640, 2006.

[66] 1 White, Martin J., Lars Hernquist, and Volker Springel. Simulating the Sunyaev-Zel'dovich effect(s): Including radiative cooling and energy injection by galactic winds. *Astrophys.J.*, 579:16, 2002.

[67] S. D. M. White. Violent Relaxation in Hierarchical Clustering. In O. Lahav, E. Terlevich, and R. J. Terlevich, editors, *Gravitational dynamics*, page 121, 1996.

[68] Wikipedia. http://en.wikipedia.org/wiki/Gravitational_lensing_formalism.

[69] Wikipedia. http://en.wikipedia.org/wiki/Weak_gravitational_lensing.

[70] WMAP Website. http://map.gsfc.nasa.gov/.

[71] Anson W.C. Wong and James E. Taylor. What Do Dark Matter Properties Tell Us About Their Mass Assembly Histories? *Astrophys.J.*, 757:102, 2012.